catalysts

MDPI

Article

High Surface Area VO_x/TiO_2/SBA-15 Model Catalysts for Ammonia SCR Prepared by Atomic Layer Deposition

Jun Shen and Christian Hess *

Eduard-Zintl-Institut für Anorganische und Physikalische Chemie, Technical University of Darmstadt, Alarich-Weiss-Str. 8, 64287 Darmstadt, Germany; jun.shen@tu-darmstadt.de

* Correspondence: christian.hess@tu-darmstadt.de

Received: 30 October 2020; Accepted: 25 November 2020; Published: 28 November 2020

Abstract: The mode of operation of titania-supported vanadia (VO_x) catalysts for NO_x abatement using ammonia selective catalytic reduction (NH_3-SCR) is still vigorously debated. We introduce a new high surface area VO_x/TiO_2/SBA-15 model catalyst system based on mesoporous silica SBA-15 making use of atomic layer deposition (ALD) for controlled synthesis of titania and vanadia multilayers. The bulk and surface structure is characterized by X-ray diffraction (XRD), UV-vis and Raman spectroscopy, as well as X-ray photoelectron spectroscopy (XPS), revealing the presence of dispersed surface VO_x species on amorphous TiO_2 domains on SBA-15, forming hybrid Si–O–V and Ti–O–V linkages. Temperature-dependent analysis of the ammonia SCR catalytic activity reveals NO_x conversion levels of up to ~60%. In situ and *operando* diffuse reflection IR Fourier transform (DRIFT) spectroscopy shows N–Hstretching modes, representing adsorbed ammonia and -NH_2 and -NH intermediate structures on Bronsted and Lewis acid sites. Partial Lewis acid sites with adjacent redox sites are proposed as the active sites and desorption of product molecules as the rate-determining step at low temperature. The high NO_x conversion is attributed to the presence of highly dispersed VO_x species and the moderate acidity of VO_x supported on TiO_2/SBA-15.

Keywords: vanadia; NO_x; NH_3-SCR; high surface area catalyst; atomic layer deposition; *operando* DRIFTS; SBA-15; mechanism

1. Introduction

The emission of nitrogen oxides (NO_x) into the atmosphere, mainly from the electric-power industry and daily traffic, brings about a tremendous threat to the environment as well as human health. As one of the major atmospheric pollutants, NO_x has attracted increasing attention in recent years. Selective catalytic reduction (SCR) of NO_x with NH_3 is proved to be the most effective technology for the removal of NO_x from stationary and mobile sources [1]. Commercial vanadia-based ammonia SCR catalysts are typically based on vanadia and tungstia (or molybdena) on TiO_2 anatase, but vanadia supported on TiO_2 has been extensively studied as a model catalyst system [2–4].

It is known from the literature, that SCR activities depend on the vanadia structure and the support material [5–7]. Mesoporous materials such as silica SBA-15 provide higher surface area than conventional powder or planar supports [8,9], and the controlled synthesis of vanadia supported on SBA-15 was reported [10,11]. However, SiO_2 supported VO_x-based catalysts were reported to show only poor SCR performance compared to titania-based systems [5,12]. On the other hand, Segura et al. studied vanadia/titania supported on SBA-15 and attributed the good catalytic NH_3-SCR reactivity to isolated VO_x or TiO_2 species [13]. Reiche et al. prepared high surface area TiO_2, SiO_2, and TiO_2-SiO_2 supported vanadia systems using sol-gel methods and selective vanadia grafting and found TiO_2-based

catalysts to show the highest SCR activity. In mixed TiO_2-SiO_2 aerogels, vanadia was reported to be preferentially grafted to Ti sites [5]. Compared to these conventional synthesis techniques, atomic layer deposition (ALD) enables accurate control at the atomic scale without damaging the structure of the original matrix [9,14–16]. Although ALD has been widely applied to metal-oxide deposition, such as SiO_2 [17–19], TiO_2 [20–24], and VO_x [9,25–29], there are only very few studies on the deposition of vanadia and titania on mesoporous SBA-15 [30], and its application to NH_3-SCR [29].

A limitation of VO_x-based catalysts for NO_x removal by NH_3-SCR is the high and narrow temperature window of acceptable deNO_x efficiencies. While VO_x/SiO_2 catalysts are characterized by a wide temperature window but extremely low NO_x conversion, attributed to the inert support and low acid site adsorption, VO_x/TiO_2 catalysts show higher NO_x conversions within a narrow temperature window (300–400 °C), resulting from the temperature dependence of the adsorption and redox reaction behavior. One may envision that combining both support materials in a controlled manner may improve the overall catalytic performance.

While there is an ongoing debate regarding various aspects of the mechanism of VO_x-based catalysts for NH_3-SCR reaction, it is now widely accepted that the majority route for the catalytic reaction is an Eley-Rideal (E-R) rather than a Langmuir-Hinshelwood (L-H) mechanism [31–33], with the overall mechanism including the following four steps: (i) NH_3 adsorption on V^{5+}=O (Lewis acid sites) or V^{5+}–OH (Bronsted acid sites), (ii) NO reacting with adsorbed NH_3 to form intermediate NH_2NO at Lewis acid sites (L acid sites) or NH_3NO at Bronsted acid sites (B acid sites), (iii) rearrangement of surface species releasing the intermediate by breaking N-H bonds and coordination bonds between the nitrogenous intermediate and its adsorption site, and by reducing the surface vanadia species from V^{5+} to V^{4+} with -OH groups or water being adsorbed, (iv) reoxidation of surface V^{4+} (V^{3+} at oxygen vacancies) by O_2 accompanied by desorption of surface H_2O [34–36], Research interests have been focused on exploring the key step(s) of the whole process on a microscopic scale and explaining the temperature-dependent relation between structure and activity. To this end, literature work may be divided into studies on the nature of the acid sites for reactants adsorption, the redox reaction step, and the desorption of products, respectively.

The first aspect, i.e., the sites for reactants adsorption (L vs B acid sites), has been a matter of debate from the beginning. In brief, L acid sites were related to V=O and B acid sites to V–OH species. Earlier, Topsoe et al. had proposed B acid sites to be the catalytically active sites as they detected a dominant amount of NH_4^+ adsorbed onto V–OH surface sites [34,37–40], On the other hand, Ramis et al. found NH_3 adsorbed on V=O sites to be thermally more stable than NH_4^+, implying that L acid sites were the dominant adsorption sites under reaction conditions [41], More recently, Marberger et al. supported the idea of Lewis acid sites being the active intermediate by observing a faster consumption of NH_3 adsorbed at L acid sites compared to NH_4^+ adsorbed at B acid sites [42,43], Zhu et al. objected to the standpoint of Lewis acid sites as active sites by concluding that minority L sites (V^{5+}=O) exhibited higher activity (TOF), while the more abundant B sites (V^{5+}–OH) dominated the overall reaction [44], Thus, still no consensus has been reached regarding the role of L and B acid sites.

The redox reaction step has been considered to be related to the reactivity and connected to the VO_x surface structures. The use of in situ electron paramagnetic resonance (EPR) and X-ray absorption spectroscopy (XAS) under reaction conditions has revealed the reducing/reoxidizing processes to be accompanied by changes of the vanadium valence and VO_x surface structure [45–48]. Feng et al. reported VO_x with polymeric structure to be redox-active and provided an atomic view of the change of the VO_x structure with redox state [49–51]. Consistently, density functional theory (DFT) results showed that formation of both oxidized and reduced VO_x, i.e., V^{5+} and V^{4+}, kept the vanadyl bond intact for isolated VO_x on TiO_2, as verified by in situ EPR data for VO_x/TiO_2 exposed to ammonia [52]. All of these results have revealed that the redox reactivity of VO_x species is structure sensitive.

Finally, we turn to the interaction between H_2O and surface VO_x sites. According to DFT calculations by Avdeev et al., adsorbed water changes the VO_x molecular configuration by spontaneous

dissociation and formation of surface V–OH groups [53–55]. Importantly, lattice oxygen of surface VO_x species was shown to originate from adsorbed water rather than gas-phase oxygen [55]. Oxygen-18 isotope labeling studies have revealed that both terminal V=O and bridging V–O–V bonds readily exchange oxygen with water vapor [56].

To date, a detailed understanding of the role of these factors and the VO_x surface structure is still missing. In our previous work, we have developed a hierarchical NH_3-SCR model catalyst using low surface area silica particles as a platform [12]. Here, we report on a new model catalyst system based on high surface area mesoporous silica SBA-15. In particular, we employ ALD for controlled synthesis of titania and vanadia layers within the pores of the silica matrix and demonstrate its catalytic activity in NH_3-SCR. Using UV-Vis and Raman spectroscopy and, in particular, in situ DRIFTS, we explore the nature of the surface sites upon exposure to different gas atmospheres and temperatures, including NH_3-SCR reaction conditions.

2. Results

2.1. Catalyst Characterization

Table 1 gives a summary of the prepared samples and their surface area and porosity characteristics. Upon ALD deposition of TiO_2 and VO_x on mesoporous silica SBA-15, surface area and pore volume drop by roughly half as reflected more precisely in Table 1, and are accompanied by a reduction in pore diameter. The observed decrease in specific surface area is attributed to a coating of the (rough) mesoporous channels but also to closure of SBA-15 micropores, as discussed previously [57]. Increasing VO_x deposition leads to a further (but much smaller) overall decrease of the specific surface area and pore volume (see Table 1). As shown in Figure S1, after TiO_2 and VO_x deposition, the nitrogen adsorption-desorption isotherms show variations of the hysteresis loop compared to bare SBA-15. In particular, the desorption branches exhibit a bulge towards lower p/p° values, indicating the presence of narrowed mesopores [58]. Thus, despite the use of ALD the pores of the silica matrix are not evenly coated, resulting in pore narrowing and possibly pore blocking, consistent with the observed overall decrease in surface area.

Table 1. Surface, porosity, and V loading characteristics of the prepared samples.

Samples	S_{total} [m^2/g]	D_p [nm]	V_{total} [cm^3/g]	L_V [V/nm^2]	V:Ti (wt%) [a]
SBA-15	952	6.96	0.82	–	–
TiO_2/SBA-15+1xVO_x	410	6.33	0.49	0.4	1.4:5.8
TiO_2/SBA-15+3xVO_x	366	6.33	0.43	1.6	5.1:5.9
TiO_2/SBA-15+5xVO_x	355	6.33	0.43	2.0	6.0:5.6

[a] From ICP-OES.

Figure 1a depicts wide-angle XRD patterns of TiO_2/SBA-15+nxVO_x (n = 1, 3, and 5) and TiO_2/SBA-15. None of the diffractograms shows any peaks, thus indicating the absence of crystalline titania and vanadia phases and confirming the amorphous nature of the SBA-15 silica matrix. The broad feature at around 23° has been attributed to the walls of mesoporous silica [59]. To check for microcrystalline domains the sample TiO_2/SBA-15+3xVO_x was examined in more detail using UV Raman spectroscopy (see Figure S2), which was shown to be a sensitive indicator for small (micro)crystalline titania contributions in our previous work [12]. According to Figure S2, there is no indication for the presence of titania microcrystals due to the absence of characteristic anatase (394, 514, and 634 cm^{-1}) and rutile (443 and 610 cm^{-1}) bands [60,61], or V_2O_5 microcrystals. In the context of Raman detection of V_2O_5, it should be mentioned, however, that visible Raman spectroscopy is typically more sensitive to V_2O_5 microcrystals than UV Raman spectroscopy (see discussion below).

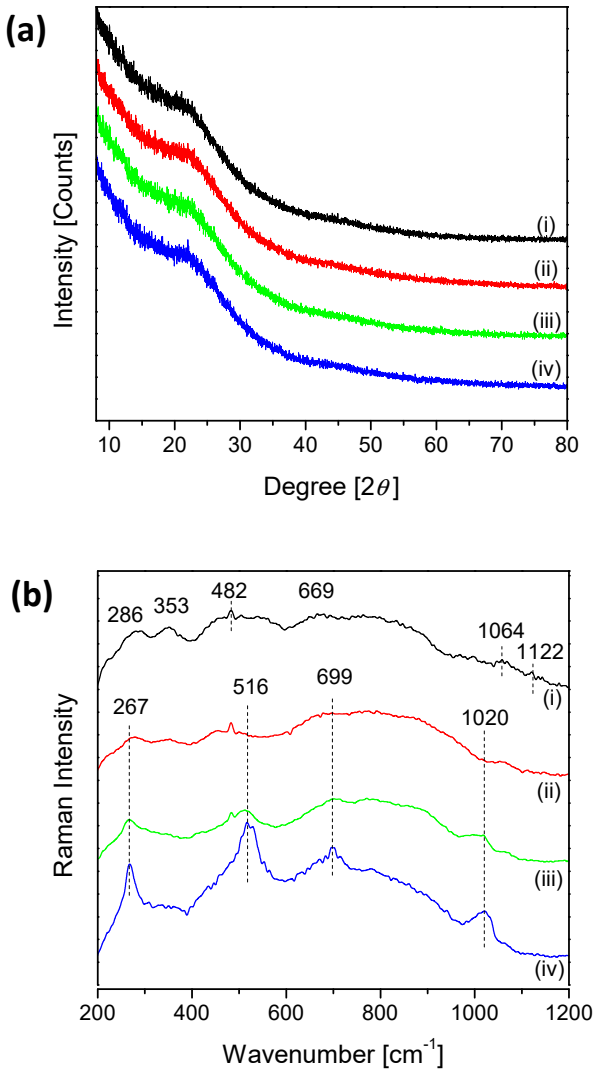

Figure 1. (**a**) XRD patterns and (**b**) Raman spectra of the samples TiO_2/SBA-15 + nxVO_x (n = 1, 3 and 5) compared to TiO_2/SBA-15 under ambient conditions. (i) TiO_2/SBA-15, (ii) TiO_2/SBA-15+1xVO_x, (iii) TiO_2/SBA-15+3xVO_x, (iv) TiO_2/SBA-15+5xVO_x.

Figure 1b shows the corresponding Raman spectra at 532 nm excitation. The spectrum of TiO_2/SBA-15 is characterized by broad features typical for amorphous silica dominating the weaker (surface) titania contributions [62]. Major features include the band at around 450–550 cm^{-1} associated with four-membered rings (D_1), and the broad band at around 600–900 cm^{-1} assigned to symmetrical Si–O–Si stretching and three-membered rings (D_2) [63]. The band located at 353 cm^{-1} is assigned to bending in Si–O–Si bridges [64], whereas the band at 286 cm^{-1} has been attributed to the A_1 mode of TiO_6 octahedra [65,66]. The small feature at 1064 cm^{-1} is characteristic of silica TO phonons [67], whereas the weak Raman peak observed at 1122 cm^{-1} for TiO_2/SBA-15 is attributed to framework Ti–O–Si species [68]. Importantly, the addition of increasing amounts of vanadia leads to the appearance of new Raman signals at around 267, 516, 699, and 1020 cm^{-1}. At first sight, the signals at around 267, 516, and 699 cm^{-1} show some similarity with those observed for crystalline V_2O_5, however, closer inspection reveals significant differences. The observed signals rather indicate the presence of hydrated vanadia forming xerogels $V_2O_5 \cdot nH_2O$, resembling those discussed previously in the context of silica-supported vanadia, and the peak at 1020 cm^{-1} is attributed to the V=O stretching vibration mode of tetrahedral VO_x species [69]. Based on the above results from XRD and Raman spectroscopic characterization, we can conclude that the ALD-prepared samples contain amorphous titania and

vanadia on silica SBA-15 and that titania at the loading studied here (2 Ti/nm^{-2}) does not form a conformal layer on the silica surface allowing vanadia to interact with titania and silica. According to a previous ALD study [29], deposition of 3 Ti nm^{-2} and 7 Ti nm^{-2} onto SiO_2 leads to the formation of sub-monolayer titania, in agreement with the results obtained here.

In the following, we will focus on the structural and catalytic properties of sample TiO_2/SBA-15+3xVO_x with a vanadium loading density of 1.6 V/nm^2. Table S1 and Figure 2 summarize the results of the XPS analysis. As shown in Table S1, Si, O, Ti, and V are detected at the catalyst surface, besides C. The Ti/Si and V/Si ratios correspond to 0.10 and 0.12, respectively, suggesting the presence of similar amounts of Ti and V on the surface. The results are consistent with the above picture of a mixed layer and rule out the exclusive formation of large titania or vanadia (3D) aggregates, which would strongly reduce the visibility of Ti and V in XPS. The left of Figure 2 depicts the O 1s, V $2p_{1/2}$, and V $2p_{3/2}$ photoemission located at 532.9 eV, 524.9 eV, and 517.4 eV, respectively. As expected, the former is dominated by the O 1s contribution from SiO_2, by comparison with the literature [69]. Detailed analysis of the V $2p_{3/2}$ region based on literature data for binary vanadia compounds (V_2O_5, V_2O_4, V_2O_3) reveals the presence of V^{5+} at 517.6 eV (60%) and V^{4+} at 516.3 eV (40%), while a small contribution from V^{3+} at 515.7 eV cannot be ruled out [70,71]. The Ti $2p_{3/2}$ peak is composed of (at least) two contributions located at 458.7 and 459.9 eV, which can be attributed to TiO_2 domains and to Ti–O–Si bonds, respectively [5,72].

Figure 3a depicts diffuse reflectance (DR) UV-Vis spectra of TiO_2/SBA-15+3xVO_x in comparison to TiO_2/SBA-15. To clarify the influence of water from ambient on the catalyst structure, spectra were recorded under ambient (hydrated) and dehydrated conditions. Please note that bare silica SBA-15 does not show any significant UV-Vis absorption. The UV-Vis spectrum of Ti/SBA-15 is characterized by strong absorption at around 280 nm, which has been attributed to charge transfer between an oxygen ligand and the central Ti^{4+} ion [73,74], whereas the position of the absorption band is consistent with higher coordinated or oligomeric titania species [75]. The presence of oligomeric species would be in agreement with the literature on SiO_2-supported titania, reporting two-dimensional oligomers of TiO_5 domain at a loading density of about 4 Ti nm^{-2}, which is higher than the density used in this work (2 Ti nm^{-2}) [76].

Regarding the vanadia structure, the observed UV-Vis absorption was analyzed based on the ligand-to-metal charge transfer (LMCT) transitions observed for bulk vanadia reference compounds [77]. To this end, bands at around 240 and 290 nm were reported to originate from isolated tetrahedrally coordinated mono-vanadate ions [78], while the bands at about 270, 340, and 412 nm were assigned to poly-vanadate ions [79]. In the literature, the bands at 308, 371, and 406 nm were assigned to LMCT transitions of monomeric tetrahedral VO_4^{3-}, oligomeric tetrahedral VO_3^-, and polymeric distorted tetrahedral VO_3^- ions, respectively [80]. It was also reported that the bands at around 440–510 nm were due to LMCT transitions of V^{5+} species with a square pyramidal structure and those at 545–650 nm were due to d-d transitions of V^{4+} species with a square pyramidal structure. For crystalline V_2O_5, a broad absorption band with maxima ranging from 440 to 490 nm was observed [77]. The presence of V^{3+} and/or V^{4+} species was shown to lead to d-d transitions ranging from 600 to 800 nm [81]. A comparison of the hydrated and dehydrated state of the sample reveals the presence of a broad band at around 380–450 nm, which has been attributed to the coordination of water to V sites leading to major structural changes [74].

After dehydration, the UV-Vis absorption behavior is characterized by contributions at around 280, 320 and 400 nm. Based on the above literature results, these are attributed to monomeric/dimeric, oligomeric, and polymeric VO_x species, respectively. The intensity increase at around 260 nm is assigned to Ti–O–Ti from Ti–OH or possibly V–O–Ti from V–OH. Because of the overlap of charge transfer bands of titania and vanadia [80,82], removal of the titania contribution facilitates the analysis of the surface vanadia structure (see Figure S3) [83]. As a result, Figure S3 shows the presence of an asymmetric broad absorption band located between 250–550 nm for the hydrated and between 250–450 nm for the dehydrated sample, together with the result of a fit analysis based on the above

reference data [83,84]. Besides, the ratio of monomeric/dimeric/oligomeric VO_x with tetrahedral coordination to polymeric VO_x with (pseudo-)octahedral coordination was estimated to increase from 0.31 to 12.5 upon dehydration, underlining the structural changes associated with the removal of coordinated water.

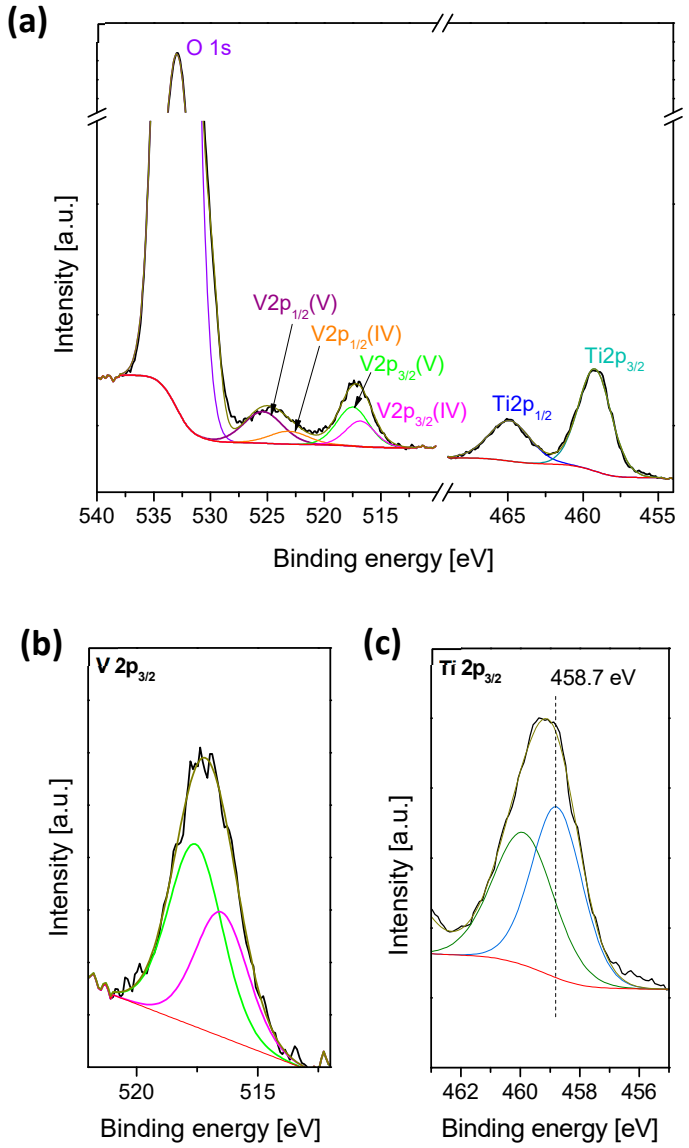

Figure 2. (**a**) O 1s, V 2p, and Ti 2p photoemission of TiO_2/SBA-15+3xVO_x. Detailed view of (**b**) the V $2p_{3/2}$ region (**c**) the Ti $2p_{3/2}$ region. The colored lines represent the result of a least-square fit analysis.

Based on the UV-Vis spectra the bandgap energy E_g was determined using the general power-law expression suggested by Davis and Mott based on the absorbance α [85].

The value of the parameter n in Equation (1) was set to 2 following the literature [82,86], showing a linear relationship when plotting $(\alpha h\nu)^{1/2}$ vs $h\nu$ (Tauc's method) [87]. Extrapolation of the linear region to $(\alpha h\nu)^{1/2} = 0$ yields E_g values of 2.99 and 3.30 eV for the hydrated and dehydrated state of the catalyst, respectively. As the E_g value is negatively correlated to the number of covalent V–O–V bonds (CVB) via the relation CVB = 14.03 − 3.95 E_g [82], an increase in E_g implies a decrease in the degree of VO_x polymerization upon dehydration:

$$\alpha h\nu \propto (h\nu - E_g)^n \quad (1)$$

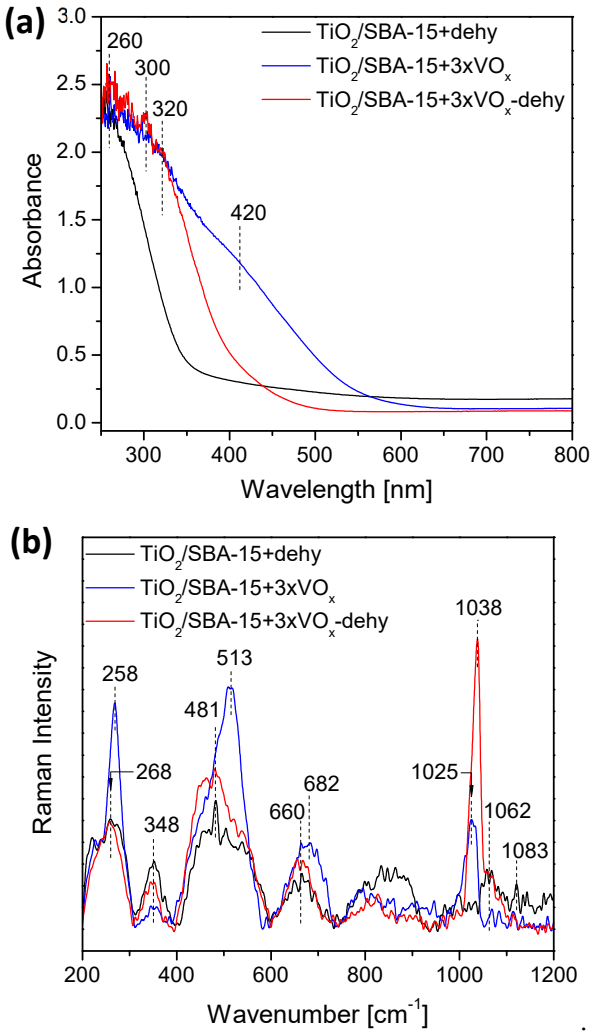

Figure 3. (**a**) DR UV-is and (**b**) Raman spectra of TiO_2/SBA-15+3xVO_x under ambient (hydrated) and dehydrated conditions in comparison to dehydrated TiO_2/SBA-15.

Figure 3b depicts Raman spectra of TiO_2/SBA-15+3xVO_x under hydrated and dehydrated conditions in comparison to the spectrum of TiO_2/SBA-15. As discussed above VO_x-related features are observed at 268, 513, 682, and 1025 cm^{-1}. Upon dehydration, the vanadyl (V=O) stretching mode shows an intensity increase and blueshift from ~1025 to 1038 cm^{-1}, consistent with previous work on VO_x/SiO_2 and $VO_x/(TiO_2 + SiO_2)$ [29,69]. The position of the V=O band at 1038 cm^{-1} in the visible Raman spectrum is characteristic for tetrahedrally coordinated vanadium ions, and has been associated with monomeric and/or small oligomeric VO_x species, consistent with the results from UV-Vis spectroscopy (see above). The presence of (micro)crystalline V_2O_5 in the dehydrated state of the catalyst can be excluded due to the absence of the characteristic vanadyl feature of V_2O_5 at 994 cm^{-1} [69]. The shoulder observed at around 1062 cm^{-1} has been attributed to V–O–Si bridging bonds [88]. The Raman bands observed at 268, 513, and 682 cm^{-1} for the hydrated state are consistent with the presence of hydrated vanadia forming xerogels $V_2O_5 \cdot nH_2O$, as discussed above. Upon dehydration, these bands disappear due to the structural transformation of surface vanadia, leading to an increased visibility of the support-related bands at 258, 481, and 660 cm^{-1} discussed below.

2.2. Catalytic Performance

The NH_3-SCR activity was examined within 100–450 °C using a mixture of 500 ppm NH_3, 500 ppm NO, 5% O_2, and N_2 (balance). The temperature was increased from 100 °C to 450 °C in 50 °C steps

keeping each temperature for 20 min for equilibration. Analysis of the gas phase at the reactor outlet was performed by quantitative FT-IR spectroscopy. Figure 4 depicts the catalytic performance for NO_x conversion over TiO_2/SBA-15+3xVO_x as a function of temperature. Table 2 summarizes the NO_x conversion and N_2 selectivity values. The NO_x conversion follows a volcano shape with an increase from 100 to 250 °C, a maximum conversion level at 250–350 °C, and a decrease above 350 °C. The large error bar in the low temperature range is related to influences of the adsorption equilibrium process on the reaction step. At high temperatures a decrease of both NO_x conversion and N_2 selectivity is observed, which may be attributed to increased NH_3 oxidation leading to N_2O generation.

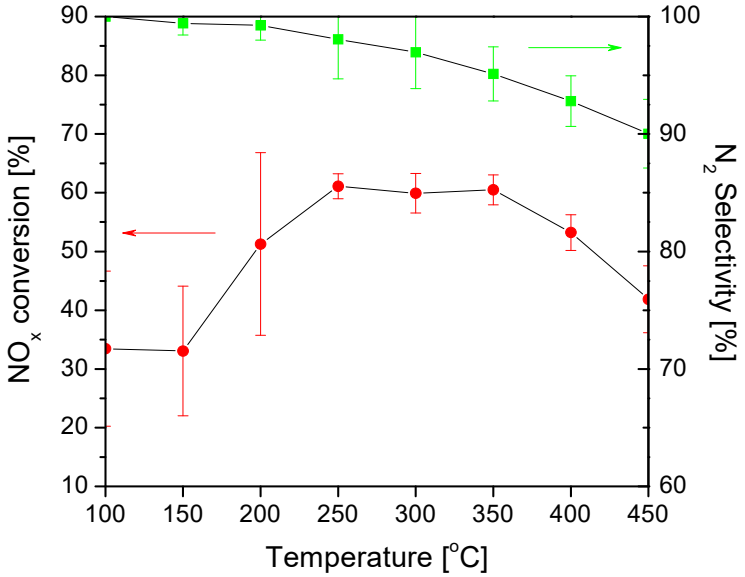

Figure 4. Catalytic performance of TiO_2/SBA-15+3xVO_x in NH_3-SCR. The temperature was increased from 100 °C to 450 °C. The feed gas consisted of 500 ppm NH_3, 500 ppm NO, and 5% O_2 balanced with N_2. The total flow rate was 50 NmL min^{-1} (GHSV = 40,000 h^{-1}).

Table 2. Catalytic performance of TiO_2/SBA-15+3xVO_x in NH_3-SCR as a function of temperature. The feed gas consisted of 500 ppm NH_3, 500 ppm NO, and 5% O_2 balanced with N_2. The flow rate was 50 NmL min^{-1} (GHSV = 40,000 h^{-1}).

Temperature, °C	**100**	**150**	**200**	**250**	**300**	**350**	**400**	**450**
NO_x conversion, %	33.4	33.1	51.3	61.1	59.9	60.5	53.2	41.9
N_2 selectivity, %	100	99.4	99.3	98.1	97.0	95.1	92.8	90.0

Despite the similar shape of the conversion, the TiO_2/SBA-15+3xVO_x sample shows significantly higher catalytic activity as VO_x/(SiO_2 + TiO_2) samples prepared by sol-gel methods [5]. In this context, it was reported that doping TiO_2 with Si may result in an increase in NO_x conversion and a decrease of the lower temperature limit from 360 °C for pure TiO_2 to 300 °C or lower for Si-doped samples [72]. Interestingly, the catalyst exhibits an excellent N_2 selectivity with values higher than 90% even at 450 °C. This behavior may be attributed to the (micro)porous structure and large surface area of the SBA-15 support, inhibiting the growth of bulk-like V_2O_5 species, which were suggested as main cause for N_2O formation [8]. In contrast to the results shown in Figure 4, VO_x/SiO_2 samples (prepared by ALD) showed only low NO conversions. In fact, the presence of titania was reported to enable V–O–Ti bond formation, which was related to the number and strength of surface acid-base sites [29]. Thus, we can conclude that besides the influence of (micro)structural effects, the improved catalytic performance may be attributed to the controlled preparation of dispersed active sites and a submonolayer of TiO_2 on SiO_2.

2.3. Operando Characterization of TiO_2/SBA-15+3xVO_x

To gain insight into the NH_3-SCR mechanism we applied DRIFTS in the presence of different gas environments and at different temperatures including reaction conditions (*operando*). Figure 5 shows DRIFT spectra of TiO_2/SBA-15+3xVO_x exposed to a gas mixture of 500 ppm NH_3, 500 ppm NO, and 5% O_2 (balanced with N_2) at different temperatures from 100 °C to 450 °C at a flow rate of 50 NmL/min. In Figure 5a, the black curve (labeled 'N_2, 300 °C') corresponds to the catalyst in a nitrogen flow at 300 °C before exposure to the reaction gas mixture. Features located at around 919 and 1036 cm^{-1} and at around 1849 and 2002 cm^{-1} have previously been assigned to V–O–V and V=O stretching modes of surface VO_x species and their first overtones, respectively [2,50,89,90]. The feature at 1203 cm^{-1} has been ascribed to L acid sites on TiO_2 [91]. The shoulder at around 1640 cm^{-1} and the broad band within the range 3500–3800 cm^{-1} can be attributed to OH bending and stretching of water, respectively [2,72]. In the OH stretching region, the sharp peak at 3745 cm^{-1} is characteristic of isolated Si–OH groups, while the small feature at 3656 cm^{-1} can be associated with V–OH [74]. The Si–OH feature shows an asymmetric broad tail at around 3650 cm^{-1}, which has been assigned to Ti–OH [92].

Upon exposure to the reaction gas mixture, two new features appeared at 1418 and 1455 cm^{-1}, which can be attributed to the asymmetric N–H bending vibration of NH_4^+ linked to B acid sites, while the shoulder and small feature at 1176 and 1606 cm^{-1} have been associated with the symmetric and symmetric N–H bending vibrations of NH_3 linked to L acid sites, respectively [93,94]. According to Figure 5a, the observed N–H modes show a different temperature-dependent behavior. Whereas the feature at 1606 cm^{-1} decreased with temperature and disappeared at about 250 °C, the band at about 1418 cm^{-1} kept intact.

In Figure 5b, upon exposure to the reaction gas mixture, new IR bands are observed at 2803 and 3050 cm^{-1}, which can be attributed to N–H stretching of NH_4^+ linked to B acid sites, while the bands located at 3159, 3278, and 3370 cm^{-1} are assigned to N–H stretching modes of NH_3 coordinated to L acid sites [41,94–96]. As the temperature increases, the bands at 3278 and 3370 cm^{-1} show an intensity decrease and completely disappear at temperatures above 300 °C, while the feature at 3159 cm^{-1} is detectable until 450 °C. Similarly, the bands at 2803 and 3050 cm^{-1} related to NH_4^+ on B acid sites can be observed within the whole temperature range.

Figure 6 depicts DRIFT spectra of TiO_2/SBA-15+3xVO_x exposed to different gas environments at 300 °C at a total flow rate of 50 NmL/min within (a) 2600–3500 cm^{-1} and (b) 3500–4000 cm^{-1}. Following the assignments discussed in the context of Figure 5, the features at 2808 and 3046 cm^{-1} are assigned to NH_4^+ coordinated to B acid sites, and those at 3150, 3275, and 3356 cm^{-1} to NH_3 bound to L acid sites (see Figure 6a).

Similarly to the effect of temperature, the bands linked to B acid sites (2808 and 3046 cm^{-1}) and the band linked to L acid sites at 3150 cm^{-1} are observed independent of the composition of the gas atmosphere, while those at 3275 and 3356 cm^{-1} can only be detected upon exposure to gas mixtures containing NH_3. That is to say, that NH_4^+ on V–OH sites is stable towards reaction no matter which redox conditions, while NH_3 adsorbed on specific L acid sites was proved to be reactive. In the corresponding high-wavenumber region (see Figure 6b) IR bands are observed at 3655 and 3737 cm^{-1} in all gas mixtures and are attributed to V–OH and Si–OH stretching vibrations, respectively, as discussed above, while the broad absorption band extending to ~3600 cm^{-1} originates from Ti–OH (see above) and the background from the fine structure of adsorbed water.

Upon closer inspection, the IR spectra in Figure 6 show gas phase-dependent variations. Upon the first exposure to 20 vol% O_2, no acid site-related bands are observed. However, water-related background peaks are detected indicating the rearrangement of surface hydroxyl groups into water under oxidizing conditions [55]. Switching to the reductive atmosphere, i.e., NH_3/NO, results in the appearance of the five N–H stretching modes related to L and B acid sites (see above), while during the following O_2 treatment the L site related features at 3275 and 3356 cm^{-1} disappear. On the other hand, the 3150 cm^{-1} band assigned to NH_3 coordinated to V=O sites, is still detected under oxidizing conditions. In the high-wavenumber region, the Si–OH, Ti–OH, and V–OH signals first

show a decrease and then a partial recovery in oxygen. Next, the catalyst was exposed separately to NH_3 and NO, and then to a NO/O_2 mixture oxidation. In the presence of NH_3 reduction, the L site related features completely reappear and the water-related peaks show a weak positive increase indicating that NH_3 itself could be reduced to NH_n thereby transferring hydrogen atoms to adjacent hydroxyl groups to form water. Upon oxidation by NO or NO + O_2 the features at 3275 and 3356 cm^{-1} disappeared, while the water-related peaks significantly increased, suggesting the promotional effect of NO regarding NH_3 oxidation, leading to intermediate formation (e.g., NH_2–NO or NH–NO), consistent with results from DFT [97], and mass spectroscopy [98].

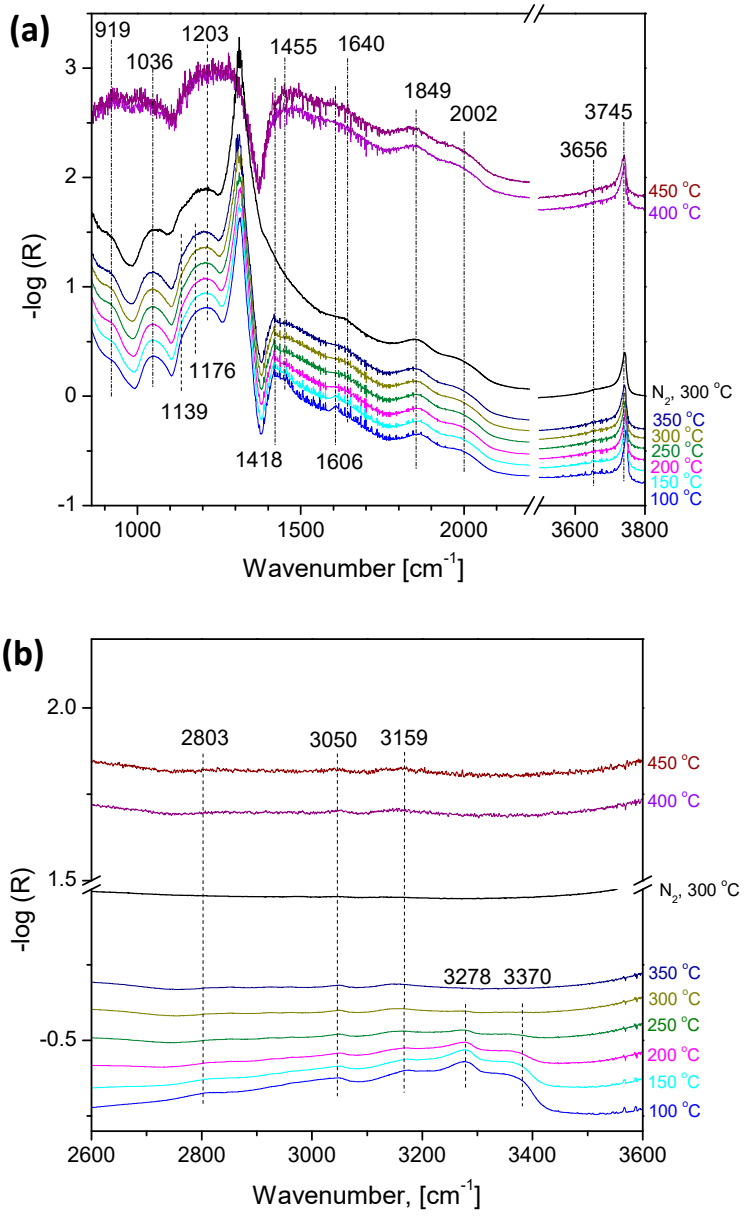

Figure 5. DRIFT spectra of TiO_2/SBA-15+3xVO_x exposed to a gas mixture of 500 ppm NH_3, 500 ppm NO, and 5% O_2 (balanced with N_2) at temperatures from 100 °C to 450 °C within (**a**) 850–3800 cm^{-1}, (**b**) 2600–3600 cm^{-1}. The total flow rate was 50 NmL/min (GHSV = 40,000 h^{-1}).

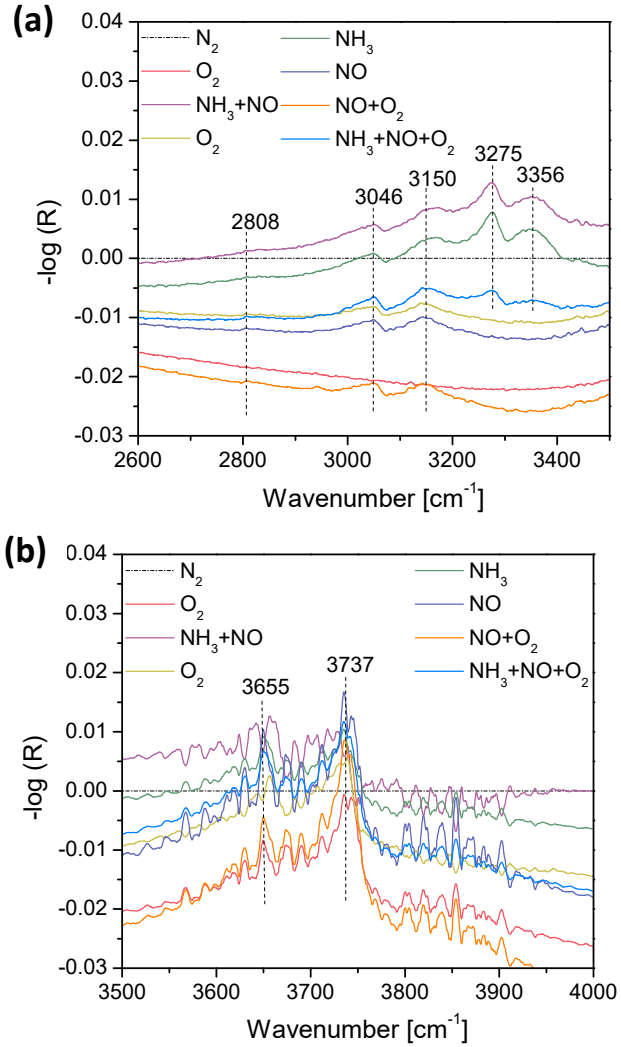

Figure 6. DRIFT spectra of TiO_2/SBA-15+3xVO_x exposed to different gas environments at 300 °C and at a total gas flow rate of 50 NmL/min (GHSV = 40,000 h^{-1}) within (a) 2600–3500 cm^{-1}, (b) 3500–4000 cm^{-1}.

Finally, the catalyst was exposed to reaction conditions, i.e., an NH_3/NO/O_2 mixture, leading to the re-appearance of all five acid site-related features, while the peaks for Si–OH, Ti–OH, and V–OH decreased in intensity. It is worth mentioning that there is a distinct difference in the IR spectra for exposure to the NH_3/NO mixture and the subsequent exposure to NH_3 and NO. In the former case, the presence of NH_3 was sufficient to competitively adsorb on the surface resulting in H_2O desorption, while in the latter case, NH_3 initially adsorbed on the surface was oxidized by NO resulting in NH_2–NO/N–NO and water formation with reduced competitive adsorption [98]. These above results are consistent with the strength of adsorption following the order NH_3 > H_2O > NH_2–NO intermediate, in agreement with the literature [99,100]. Interestingly, the addition of oxygen (NH_3/NO/O_2) leads to a different, distinct state of the catalyst regarding the presence of surface species, which falls between the behavior observed for NH_3 exposure and subsequent exposure to NH_3 and NO, and is also different to that obtained by subsequent exposure to NH_3/NO and oxygen.

In summary, the DRIFTS results shown in Figures 5 and 6 reveal important differences in the adsorption/reactivity behavior of NH_3 species attached to acid sites. The N–H stretching linked to B acid sites at 2803 and 3050 cm^{-1}, which have been assigned to coordinate and suspended N–H bonds [41], respectively, did not respond to the different atmospheres and different temperatures, suggesting that the B acid sites were active for adsorption but not for reaction. On the other hand, the L acid site related N-H stretching features at 3275 and 3356 cm^{-1}, assigned to -NH_2 and -NH species,

showed a more distinct response to the nature of the gas environment and the temperature, while the 3150 cm^{-1} feature, assigned to adsorbed NH_3 species, remained passive towards reaction. Regarding the reaction mechanism, we draw the following conclusions: (a) NO reacts with NH_3 connected to the inert site (3150 cm^{-1}). (b) NH_3 adsorbs to active L acid site forming NH_2 by H-abstraction (3275 and 3356 cm^{-1}), followed by its interaction with NO leading to NH_2NO intermediate formation and further reaction to N_2 and H_2O. (c) In case of N_2O formation, NH_2NO may be expected to lead to NHNO intermediates and finally N–NO.

Figure 7 depicts the results of the in situ detection of the exhaust gas during different temperature SCR experiments from 100 to 450 °C. Each temperature was kept for 20 min to reach an equilibrium state. When increasing the temperature, desorption peaks were observed indicating changes in the surface concentration as a function of temperature. At lower temperatures, the presence of NH_3 peaks but absence of NO desorption peaks (not shown) suggests a surface reaction following the E-R rather than the L-H route, in agreement with the literature [32,33]. In addition, insight into the reaction mechanism can be obtained. To this end, three steps have been distinguished, i.e., adsorption of reactants (mainly NH_3), reaction, and desorption of products (such as H_2O, NO_2, and N_2O). According to Figure 7, there are low temperature desorption peaks of NH_3 at 25/100 °C and 100/150 °C, which are attributed to NH_3 desorption from the B acid site, while high temperature NH_3 peaks above 150 °C are assigned to desorption from L acid site [5,101,102]. These peaks disappeared at about 300/350 °C, consistent with the disappearance of L acid sites in DRIFTS (see Figure 5). The strong water desorption peak at 25/100 °C originates from condensation of OH groups, e.g., after desorption of NH_3 bound to B acid sites [5]. The first desorption peak of NO_2 at 150/200 °C can be attributed to the distortion and release of NO_2 from nitrite/nitrate species by NO molecules connected to surface oxygen sites [103,104]. The second peak at 200/250 °C shows that NO oxidation is faster than NO_2 desorption at 200 °C. Similarly, the first desorption peak for N_2O detected at 200/250 °C is indicative of its formation on active sites and subsequent chemisorption at temperatures <250 °C [105].

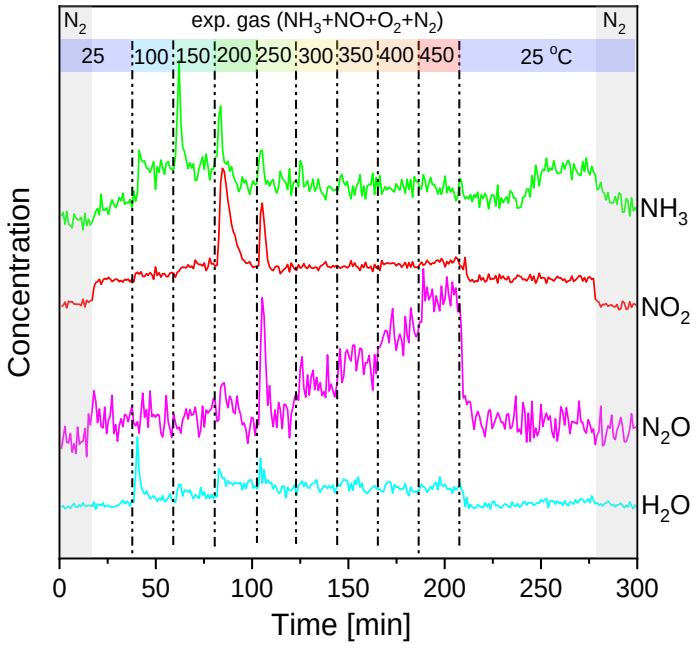

Figure 7. In situ detection of the exhaust gas during NH_3-SCR reaction of TiO_2/SBA-15+3xVO_x at 100–450 °C. The feed consisted of 500 ppm NH_3, 500 ppm NO, and 5% O_2 (balanced with N_2) at a total flow rate of 50 NmL/min (GHSV = 40,000 h^{-1}).

All in all, catalyst characterization of TiO_2/SBA-15+3xVO_x reveals a relatively high surface area (>350 m^2/g) and the presence of surface hybrid V–O–M bonds connecting the vanadia aggregates to the substrate. The NH_3-SCR catalytic performance follows a volcano shape with temperature, with an optimal deNO_x value of about 60% at 300 °C. Finally, the *operando* DRIFTS results reveal N–H stretching features related to B and L acid sites.

3. Discussion

3.1. Surface Vanadia Structure

Previously, highly dispersed vanadia and titania on SBA-15 have been studied in detail under hydrated and dehydrated conditions [74]. Despite the lower loading ranges discussed (V: 0.00001–0.7 V/nm^2; Ti: 0.001–0.7 Ti/nm^2) valuable structural information for the present sample (1.6 V/nm^2; 2 Ti/nm^2) was obtained regarding the nature of the surface species, in particular, as all samples are well below monolayer coverage [26,106,107]. This is supported by the absence of Raman features due to crystalline V_2O_5 and TiO_2, implying the presence of amorphous domains, consisting of dispersed titania and vanadia species on the silica surface. On the other hand, the detailed surface composition after successive deposition of titania and vanadia needs closer examination, especially as it was reported that vanadium is preferentially deposited on titanium sites [26,108].

For TiO_2 deposited on SBA-15, the Ti loading was quantified as 2 Ti/nm^2, which is significantly below monolayer coverage (6–8 Ti/nm^2) [106]. DR UV-Vis spectra show an absorbance band at about 260 nm, attributed to titanium in 5-fold coordination (see Figure 3) [76]. The UV-Vis edge energies were determined to be 3.2 and 3.0 for the hydrated and dehydrated state, respectively. Comparison with edge energies of titania structures ranging from isolated tetrahedrally coordinated TiO_4 (4.3 eV) to oligomeric TiO_5 species (3.4 eV), suggests the presence of oligomeric TiO_5 species in the VO_x/TiO_2–SiO_2 sample. Regarding the effect of water on the titania structure, no difference was found between the dehydrated and hydrated state at extremely low Ti loading (<0.05 Ti/nm^2), in contrast to higher loadings (> 0.1 Ti/nm^2) [74]. In fact, adsorbed water was reported to interact with adjacent titanium atoms (Ti–O–Ti) in oligomeric titania, leading to an edge energy 0.2 eV higher than in the dehydrated state, consistent with the behavior observed here [74]. High temperature calcination is expected to lead to an increase in Ti–O–Ti linkages as part of domain TiO_2 [26] without formation of crystalline TiO_2, as discussed above (see above). While anatase and rutile related Raman bands are absent, the feature at 286 cm^{-1} is attributed to TiO_6 octahedra as part of amorphous TiO_2 domains on the silica surface.

After vanadia deposition, adsorption-desorption isotherms are characterized by a steep hysteresis, attributed to cavitation-controlled evaporation in a narrow range of the pore neck, while some pore blockage or seepage may not be excluded. The surface area shows only a small decrease with increasing VO_x deposition, while no significant differences in the NLDFT pore-size distribution were observed. This behavior implies that the ALD deposited VO_x did not block the pore openings, but was rather selectively deposited inside the matrix on TiO_2 domain sites, forming ink-bottle pore [109].

Although the ALD method permitted the vanadium precursor to react with all surface adsorption sites, including Ti–OH and Si–OH hydroxyls, preferential deposition seems to be inevitable [29]. According to Table 1, the sample with 1xVO_x deposition shows a lower V:Ti ratio of 0.24, at which vanadium is expected to be mainly loaded on TiO_2 domains [26]. For the 3xVO_x and 5xVO_x samples close to unit V:Ti ratios of 0.85 and 1.08 are observed, which can be interpreted as sub- and over-saturated coverage of VO_x on TiO_2, respectively. It should be mentioned that the VO_x deposition rate showed differences among the three samples. In fact, based on the growth rate for 1xVO_x, leading to a V/Ti ratio of 0.24, the extrapolated V/Ti ratio for 3xVO_x should be 0.72, which is slightly smaller than the actual value of 0.85, while the extrapolated V/Ti ratio for 5xVO_x should be 1.20, a value slightly larger than the observed value of 1.08. The increase in VO_x growth rate is attributed to a change in deposition site from titania to silica when approaching TiO_2 saturation coverage. On the other, the mobility of surface VO_x species was reported to reach its lowest surface free energy (SFE) at

elevated temperature under reaction conditions, resulting in a two-dimensional spreading of VO_x species on silica and titania [110,111]. To this end, it is worth mentioning that the IR spectra recorded at elevated temperature under reaction conditions reveal a hydroxyl signal at 3740 cm^{-1} due to surface Si–OH groups (see Figure 5), indicating that the deposition of TiO_2 and VO_x did not lead to complete coverage of the silica surface.

The UV-Vis DRS and Raman spectra provide structural information on the VO_x surface species (see Figs. 3 and S3). It is well known that the structure of surface VO_x depends sensitively on the gas environment [112]. UV-Vis spectra of the hydrated state are characterized by a 250–550 nm band, consistent with polymeric VO_x with pseudo-octahedral coordination, and by a band at 250–450 nm for the dehydrated catalyst, reflecting the presence of tetrahedrally coordinated oligomeric VO_x species, overlapping with the signal of the TiO_2/SiO_2 substrate in the dehydrated state. The presence of H_2O can hydrate the surface VO_x species leading to the formation of $V_2O_5{\cdot}nH_2O$-like gels, as evidenced by Raman features at 267, 516, 699, and ~1020 cm^{-1} under ambient conditions (see Figures 1 and 3). Regarding the position of the V=O stretching bands (~1020 and 1038 cm^{-1}) also the effect of moisture needs to be taken into account [69]. Upon dehydration, a 13 cm^{-1} blueshift of the V=O feature is observed (see Figure 3), consistent with the literature [69], leading to the formation of tetrahedrally coordinated vanadium ions. In the dehydrated state, the position of the V=O band at 1038 cm^{-1} is located between the values 1031 cm^{-1} and 1042 cm^{-1} reported for bare TiO_2 and SiO_2, respectively [29,113,114], suggesting the simultaneous existence of vanadia species on both oxides attached via V–O–Ti and V–O–Si bands.

Summarizing, regarding the structure of the VO_x surface species we propose based on our findings that (i) titania is dispersed on the silica surface in domains containing low oligomerized TiO_5, (ii) VO_x is preferentially deposited on titania sites at low VO_x loadings ($1xVO_x$), inducing the formation of dispersed oligomeric species, (iii) increasing VO_x loading results in the deposition of V on both Ti and Si sites ($3xVO_x$, $5xVO_x$).

3.2. Rate-Determining Step

In agreement with the literature, the observed temperature-dependent efficiency for NO removal follows a volcano shape, with a maximum NO conversion at 250–350 °C. N_2 selectivities are near 100% within 100–300 °C and decrease to 90% as temperatures rise to 450 °C (see Figure 4).

The reason for the reactivity changing with temperature was related to the different processes determining the rate. Generally, the SCR reaction process on the VO_x catalyst could be divided into three steps, i.e., adsorption of reactants, redox reaction, and desorption of products. On the one hand, it was stated that the redox reaction was rate-determining at low temperature, while adsorption of NH_3 on surface acid sites was the rate-determining step (RDS) at high temperature [5,115]. On the other hand, desorption of generated H_2O was considered the low-temperature RDS, and the reductive reaction of NH_3 the high-temperature RDS [116]. To explore possible structural factors related to catalytic reactivity, *operando* DRIFT was applied.

Based on the DRIFT spectra in Figures 5 and 6 part of the L acid sites are proposed as active sites, due to their gas phase and temperature dependent behavior. These sites can be associated with the N-H stretching of coordinated amide, while the stable L acid sites can be related to the N–H vibration of coordinated NH_3. Thus, the detailed H-abstraction ability is important even for the same type of adsorption sites. According to the literature, dispersed oligomeric VO_x species are believed to be the main active species, providing oxygen (V=O or V–O–V) [7,56,117,118], for H-abstraction of adsorbed NH_3 to form an amide intermediate [98]. To this end, the samples TiO_2/SBA-15-$3xVO_x$ and TiO_2/SBA-15-$5xVO_x$ with a larger fraction of oligomeric VO_x show a better NO_x conversion than TiO_2/SBA-15-$1xVO_x$ (not shown). Also, the changes of the acid site-related signals with increasing temperature demonstrate that at temperatures < 300 °C the H-abstraction step is slower than the adsorption of NH_3 (see Figure 5). The presence of adsorbed NH_3 at low temperatures was evidenced by NH_3 desorption peaks. On the other hand, desorption of water was observed at very low temperatures, indicating that its desorption was slower than its formation by reaction. Thus, we propose the RDS at

low temperatures to be related to the desorption of products, especially water. To this end, additional water vapor was reported to suppress the reactivity irreversibly, indicative of the occupation of active sites by water [72]. Our conclusions are also supported by the fact that N_2O formed at temperatures below 200 °C was adsorbed on the surface rather than being released into the gas phase.

Except for the redox properties surrounding the acid site, the acid strength is another important factor concerning the SCR reaction, relevant for both the adsorption of reactants (mainly NH_3 in E-R route) and the desorption of products (such as H_2O, NO_2, and N_2). The acidity of binary oxides and ternary oxides $VO_x/TiO_2/SiO_2$ has been the subject of previous studies, both on solid solutions and supported systems [5,29,30,108]. For binary systems, the surface acidity was found to increase as $VO_x/SiO_2 < TiO_2/SiO_2 < VO_x/TiO_2$ [30]. Regarding $VO_x/TiO_2/SiO_2$ systems prepared by ALD [29], samples with lower VO_x loading (1 V/nm^2, 3 Ti/nm^2) and higher VO_x loading (2 V/nm^2, 3 Ti/nm^2) were compared towards their acidity behavior, showing a decrease (increase) in weak/medium (strong) strength acid sites with loading. Furthermore, strong acid sites were assigned to VO_x species on titania and weak acid sites to VO_x species on silica [29]. In our study, NH_3 desorption peaks for TiO_2/SBA-15+1xVO_x were detected at higher temperature as compared to 3xVO_x and 5xVO_x (see Figure S4), consistent with the formation of stronger acid sites at lower V loading on titania. The N_2O desorption signal also follows the trend of the VO_x acid sites as 1xVO_x > 3xVO_x > 5xVO_x. For the 1xVO_x sample, even at 300/350 °C, a weak N_2O desorption peak was detected. The 3xVO_x and 5xVO_x samples showed a very similar desorption behavior of reactants and products. At temperatures > 300 °C, no more desorption of NH_3 but an increase in the N_2O concentration was detected, reflecting an increase in the H-abstraction ability. Thus the RDS at high temperatures may be related to the adsorption of NH_3.

3.3. Structure-Activity Relationship

In the sections above, we discussed the structure of VO_x loaded on TiO_2/SBA-15 and several aspects affecting the NH_3-SCR activity. Compared to previous VO_x-based model systems with similar V loading on SiO_2, TiO_2, or SiO_2 + TiO_2 prepared by other techniques, our VO_x/TiO_2/SBA-15 catalyst shows an improved NO_x conversion and operation window [5,119–121]. For NH_3-SCR over supported VO_x catalysts, high reactivity has been related to crystalline (anatase) TiO_2 [5,122,123]. Mixing SiO_2 with TiO_2, to be used as support for vanadia, introduces extra acid sites, and is accompanied by the transformation of crystalline into amorphous titania, resulting in a decrease in the catalytic performance compared to bare titania [5,124]. However, by adjusting the Si/Ti ratio, a volcano-shape of the SCR reactivity with Si content was obtained [124], indicating synergetic effects regarding the reactivity, possibly related to the presence of Ti–O–Si surface sites. Kobayashi et al. studied the acidity of TiO_2–SiO_2 mixed systems, also showing a volcano-shaped relationship as a function of composition, with a maximum at a Si/Ti ratio of 1 [124]. On the other hand, according to other studies, using the same sol-gel method, the best SCR activity was observed for lower Si/Ti ratios such as 2/8 [72,124]. The mismatch between the acidity and reactivity may be explained by the RDS discussion above, as within the low and medium temperature range, the desorption step was rate determining for the strong acid sites. In present work, ALD deposition of TiO_2 onto SiO_2 results in the formation of oligomeric TiO_2 domains, with a limited boundary between TiO_2 and SiO_2, in contrast to the more uniform mixture of Ti and Si obtained by the sol-gel method. The improved catalytic performance of the TiO_2/SBA-15+3xVO_x compared to other SiO_2/TiO_2-based VO_x catalysts can therefore be explained by the comparable amounts of V and Ti, allowing V to be deposited on TiO_2 and boundary sites (Ti–O–Si). This leads to the formation of VO_x species supported by hybrid sites (V–O–Ti, V–O–Si), thus increasing the total number of acid sites. Consistent with this scenario, for lower V loading (1xVO_x), significantly lower NO_x conversion is observed (not shown), due to the preferential deposition of V on (amorphous) TiO_2, while for higher V loading (5xVO_x), a similar behavior as for the 3xVO_x catalyst was obtained, due accessibility of both TiO_2 and Ti–O–Si boundary sites.

Meanwhile, it is well-known that the SCR reactivity of VO_x/TiO_2 catalysts shows a narrow temperature window within the high temperature range, strongly decreasing below 300 °C [125], VO_x/SiO_2 catalysts are characterized by low SCR reactivity but a wider temperature adaptability even at low temperatures [126]. Besides, according to the literature, produced H_2O was adsorbed on surface active sites because the activation barriers of the NH_2NO decomposition on the catalyst surface were much lower than those calculated for the gas-phase reaction [127]. Thus, in the low temperature range, the desorption of water and other product molecules was considered rate-determining. Keranen et al. reported that VO_x supported on pure TiO_2 led to a larger number of strong acid sites but less weak/medium ones than on a mixture of TiO_2 and SiO_2 [29], implying strong adsorption of NH_3 and H_2O. In fact, Figure 7 reveals the appearance of desorption peaks of water during heating steps. Thus, a limited mixture of TiO_2 and SiO_2 decreases the surface acid strength, facilitates desorption of H_2O and other products and is therefore expected to improve the SCR activity at low temperatures.

Another aspect that is proposed to influence the low-temperature SCR performance is the preparation of the TiO_2 domains on the SiO_2 support [26]. In contrast to other methods used for the preparation of mixed SiO_2 + TiO_2 supports, such as sol-gel based synthesis [5] and co-precipitation [124], the ALD approach enables controlled deposition of sub-monolayer titania and vanadia, resulting in micro-domain areas of TiO_2 and well dispersed VO_x species. The deposition of VO_x on small domains of an oxide less reducible than vanadia but more reducible than the support is expected to improve the dispersion of surface VO_x species [128]. Furthermore, the high surface area of the mesoporous matrix can be largely preserved by the low-temperature ALD approach and allows to further increase the VO_x loading for higher SCR catalytic performance.

4. Experimental

4.1. Chemicals

The chemicals used for the preparation of SBA-15, including triblock copolymer Pluronic P123 (molecular weight = 5800, $EO_{20}PO_{70}EO_{20}$) and tetraethylorthosilicate (>99%, TEOS), were purchased from Sigma-Aldrich Chemie GmbH (Munich, Germany). As ALD precursors for TiO_2 and VO_x, titanium tetrachloride (>99%, $TiCl_4$) and vanadium oxytrichloride (>99%, $VOCl_3$) were employed, respectively, which were purchased from Sigma-Aldrich Chemie GmbH (Munich, Germany). As oxygen source in the ALD process demineralized water was used.

4.2. Synthesis

For the preparation of SBA-15 [129], 4.0 g P123 was completely dispersed in a mixture of 120 mL HCl solution (2 M) and 30 mL water in a PP bottle at 35 °C with 250 r/min stirring for 2 h. Then 10 mL TEOS was added at 35 °C with 400 r/min stirring for 20 h. After that, the bottle was put in an oven at 85 °C with hydrothermal crystallization treatment for 24 h. Using vacuum filtration, the as-made SBA-15 was collected, followed by calcination to remove the template P123 in a muffle furnace heated to 550 °C for 12 h (heating rate: 1.5 °C/min).

VO_x/TiO_2/SBA-15 samples were prepared by ALD using a deposition system described in detail elsewhere [12]. Briefly, three ALD cycles of titania were deposited onto silica SBA-15. Finally, VO_x was deposited with 1, 3, and 5 cycles leading to different V loadings. For the ALD of TiO_2, the $TiCl_4$ precursor was evaporated in a feeding bottle at 40 °C and reacted in the reaction chamber at 120 °C for 60 s. Similarly, for VO_x ALD, the $VOCl_3$ precursor was evaporated at 40 °C and reacted at 60 °C for 60 s. In both processes, water at room temperature acted as oxidant. Between reaction steps the system was purged (N_2, 60 s).

The sample with 3 cycles of TiO_2 on SBA-15 is labeled as 'TiO_2/SBA-15', and samples with different cycles of VO_x on TiO_2/SBA-15 as 'TiO_2/SBA-15+nxVO_x' (n = 1, 3, 5). Hydrated samples correspond to samples exposed to ambient conditions for at least one week after synthesis. Samples labeled as

'dehydrated' were heated at 500–600 °C for 1 h under a controlled atmosphere (20% O_2/80% N_2) and then cooled to room temperature.

4.3. Catalytic Performance

The SCR performance was measured in a commercial reactor (CCR1000, Linkam Scientific Instruments, Tadworth, UK) in combination with quantitative gas-phase FT-IR spectroscopy, employing a Tensor 27 instrument equipped with a deuterated and L-alanine-doped triglycine sulfate (DLaTGS) detector (Bruker, Mannheim, Germany). Using mass-flow controllers, the inlet gas concentration was adjusted to 500 ppm NO, 500 ppm NH_3, and 5% O_2 (balanced with N_2), by mixing 2000 ppm NO/N_2 (±0.25% abs.), 2000 ppm NH_3/N_2 (±0.25% abs.), O_2 (≥99.999%), and N_2 (≥99.999%). During the NH_3-SCR process, the contents of NO, NH_3, and O_2 in the feed were set to 500 ppm, 500 ppm, and 5%, respectively, balanced with N_2. The weight of the catalyst sample in the reactor bed was 15 mg and the gas mixture passed through the catalyst bed at a flow rate of 50 NmL·min^{-1}, resulting in a gas hourly space velocity (GHSV) of 40,000 h^{-1}. The temperature was increased from 100 °C to 450 °C at 50 °C steps. Each temperature was kept for 20 min to allow for equilibration. The outlet gas mixture was analyzed by an FT-IR spectrometer equipped with a low volume gas cell (25 mL, LFT, Axiom Analytical, Inc, Tustin, CA, USA). The gas cell was heated to 120 °C to avoid the condensation of water produced by the catalytic reaction. IR spectra were continuously recorded with a resolution of 4 cm^{-1}. For quantitative analysis of the IR active gas-phase components (NO, NO_2, NH_3, N_2O) calibration curves were recorded.

By combining the outlet concentrations of NO, NO_2, N_2O, and NH_3 with the inlet concentrations, the N_2 concentration was calculated based on nitrogen mass conservation, assuming that nitrogen was present only as gas-phase molecular species. The NO_x conversion and N_2 selectivity were calculated using the following Equations (2) and (3):

$$NO_x \text{ conversion } = \frac{[NO_x]_{in} - [NO_x]_{out}}{[NO_x]_{in}} \cdot 100\% \quad (2)$$

$$N_2 \text{ selectivity } = \frac{2[N_2]_{out}}{[NO_x]_{in} - [NO_x]_{out} + [NH_3]_{in} - [NH_3]_{out}} \cdot 100\% \quad (3)$$

where the subscripts 'in' and 'out' represent the inlet and outlet flow, respectively.

4.4. Characterization

N_2 adsorption-desorption measurements were carried out on a NOVA 3000e system (Quantachrome, Boynton Beach, FL, USA) to determine the specific surface area using the Brunauer-Emmett-Teller (BET) method and the porosity characteristics using non-local density functional theory (NLDFT). Quantification of the vanadium content of the samples was done by inductively coupled plasma optical emission spectroscopy (ICP-OES).

XRD experiments were carried out in transmission geometry on an X-ray powder diffractometer (StadiP, Stoe & Cie GmbH, Darmstadt, Germany) with a Mythen 1K (Dectris, Baden-Daettwil, Switzerland) detector. For the measurements, a Cu Kα1 radiation (λ = 1.540598 Å) and a Ge [110] monochromator was employed.

XP spectra were recorded on an SSX 100 ECSA spectrometer (Surface Science Laboratories Inc., Minneapolis, MN, USA), equipped with a monochromatic Al-K$_\alpha$ X-ray source (1486.6 eV), in a constant analyzer energy (CAE) mode at a 36° detection angle with 0.1 eV resolution. Data analysis included subtraction of a Shirley background and a peak-fit analysis using Gaussian−Lorentzian product functions with 45% Lorentzian share. Atomic concentrations were calculated using the following relative sensitivity factors (RSFs): 0.537 (C 1s), 2.930 (O 1s), 0.817 (Si 2p), 7.810 (Ti 2p), and 9.660 (V 2p).

UV-Vis diffuse reflectance spectroscopy (UV-Vis DRS) was carried out on a V-770 spectrometer (Jasco, Pfungstadt, Germany) equipped with a praying mantis mirror cell and a high-temperature

reaction chamber (Harrick Scientific Products Inc., Pleasantville, NY). Halogen and deuterium lamps were used as light sources in the Vis and UV, respectively. A Peltier-cooled PbS detector was employed for detection. Spectra were recorded from 800 to 200 nm with a spectral resolution of 0.5 nm. MgO was used as a white standard.

Visible Raman spectra (532 nm excitation) were recorded on a Holo Spec f/1.8i spectrometer (Holographic Imaging Spectrograph, Kaiser Optical Systems, Los Altos, CA, USA) equipped with a transmission grating and a charge-coupled device (CCD) detector. 532 nm radiation obtained by frequency doubling from a Nd:YAG laser (Cobolt Inc., Kassel, Germany) was employed for excitation. The spectrometer was calibrated by the emission lines of a standard argon lamp. The laser power was set to 1.6 mW at the position of the sample as measured by a power meter (Ophir, North Logan, UT, USA).

UV Raman spectra (256.7 nm excitation) were performed with a tunable Ti:sapphire solid-state laser (Indigo-S, Coherent, Santa Clara, CA, USA). The Raman scattered light was dispersed in a three-stage spectrometer (TriVista 555, Princeton Instruments, Krailing, Germany) used in subtractive mode and detected by a charged coupled device (CCD) camera (Spec10:2KBUV, Princeton Instruments, Krailing, Germany), cooled to −120 °C with liquid nitrogen. The spectral resolution was 1 cm^{-1}. All spectra were recorded at room temperature by irradiating the samples for 900 s with a laser power of 2.6 mW at a repetition rate of 5 kHz.

DRIFTS was carried on a Vertex 70 spectrometer (Bruker, Mannheim, Germany) equipped with a liquid N_2 cooled mercury-cadmium-telluride (MCT) detector and a commercial Harrick cell (Harrick Scientific Products Inc., Pleasantville, NY, USA). As a background standard, KBr powder was used. The spectral resolution of DRIFTS was set to 1 cm^{-1}. Blank spectra were recorded by passing pure N_2 through the loaded sample, and the actual gas-phase spectra were obtained by subtracting the blank spectra. For *in situ/operando* experiments, the gas phase at the outlet of the cell was continuously analyzed by quantitative FT-IR spectroscopy as described above.

5. Conclusions

An NH_3-SCR model catalyst was prepared by controlled deposition of titania and vanadia onto a mesoporous high surface area silica support by use of ALD. The final VO_x/TiO_2/SBA-15 catalyst retained a large surface area, characterized by domains of amorphous titania on silica and the formation of dispersed oligomeric VO_x surface species. The presence of similar amounts of deposited Ti and V allows vanadium to be anchored to both TiO_2 and Ti–O–Si boundary sites, thus increasing the total number of acid sites.

Compared to other catalysts with similar composition, the SBA-15-based catalyst used in the present study shows a better NH_3-SCR performance and a wider temperature window for operation. The superior catalytic behavior is attributed to several factors, including the controlled ALD synthesis, which leads to a high dispersion of VO_x oligomeric species due to the high surface area of the mesoporous matrix. Considering the analysis of the RDS at low temperature, desorption of products is of great importance due to their strong interaction with acid sites. The structure of VO_x species with amorphous TiO_2 domains on the SiO_2 substrate, forming hybrid supports of V–O–Ti and V–O–Si, provided more acid sites, especially weak acid sites, thus leading to a better catalytic SCR performance than VO_x/TiO_2 and also VO_x on atomically mixed SiO_2 + TiO_2 supports prepared by sol-gel methods.

Our findings demonstrate the potential of using high surface area VO_x/TiO_2/SBA-15 model catalysts for gaining new insight into the factors determining the mode of operation of supported vanadia catalysts used for NH_3-SCR.

Supplementary Materials: The following are available online at http://www.mdpi.com/2073-4344/10/12/1386/s1, Figure S1. N_2 adsorption-desorption isotherms of TiO_2/SBA-15+$n$$VO_x$ (n = 1, 3, and 5) materials and SBA-15, Figure S2. UV-Raman (256.7 nm) of the TiO_2/SBA-15+3xVO_x sample. Prior to VO_x deposition the TiO_2/SBA-15 sample was calcined at 500 °C for 2 h, Table S1. Results of the XPS analysis of TiO_2/SBA-15+3xVO_x, Figure S3. UV-Vis DRS of TiO_2/SBA-15+3xVO_x sample using TiO_2/SBA-15 as the reference background. (a) hydrated, (b) dehydrated, Figure S4. *In situ* detection of the exhaust gas during NH_3-SCR reaction over(a) TiO_2/SBA-15+1xVO_x and

(b) TiO_2/SBA-15+5xVO_x catalysts at 100–450 °C. The gas feed consisted of 500 ppm NH_3, 500 ppm NO, and 5% O_2 (balanced with N_2). The total flow rate was 50 NmL/min (GHSV = 40,000 h^{-1})

Author Contributions: Original idea, C.H.; Conceptualization, J.S. and C.H.; methodology, J.S.; formal analysis, J.S.; writing—original draft preparation, J.S.; writing—review and editing, C.H.; supervision, C.H.; project administration, C.H. All authors have read and agreed to the published version of the manuscript.

Funding: This research was funded by Deutsche Forschungsgemeinschaft (DFG-FOR1583) And the APC was funded by the German Research Foundation and the Open Access Publishing Fund of the Technical University of Darmstadt.

Acknowledgments: The authors thank Karl Kopp for performing the XPS analysis, Martin Brodrecht for N_2 adsorption-desorption measurements, Kathrin Hofmann for XRD measurements, as well as Anastasia Filtschew for assistance with the DRIFT spectrometer. Financial support by the Deutsche Forschungsgemeinschaft (DFG-FOR1583) is gratefully acknowledged. We furthermore acknowledge support by the German Research Foundation and the Open Access Publishing Fund of the Technical University of Darmstadt.

Conflicts of Interest: The authors declare no conflict of interest.

References

1. Lai, J.K.; Wachs, I.E. A Perspective on the Selective Catalytic Reduction (SCR) of NO with NH_3 by Supported V_2O_5–WO_3/TiO_2 Catalysts. *ACS Catal.* **2018**, *8*, 6537–6551. [CrossRef]
2. Putluru, S.S.R.; Schill, L.; Godiksen, A.; Poreddy, R.; Mossin, S.; Jensen, A.D.; Fehrmann, R. Promoted V_2O_5/TiO_2 catalysts for selective catalytic reduction of NO with NH_3 at low temperatures. *Appl. Catal. B Environ.* **2016**, *183*, 282–290. [CrossRef]
3. Zhang, S.; Zhong, Q.; Wang, Y. Effect of rutile phase on V_2O_5 supported over TiO_2 mixed phase for the selective catalytic reduction of NO with NH_3. *Appl. Surf. Sci.* **2014**, *314*, 112–118. [CrossRef]
4. Zhu, M.; Lai, J.K.; Tumuluri, U.; Ford, M.E.; Wu, Z.; Wachs, I.E. Reaction Pathways and Kinetics for Selective Catalytic Reduction (SCR) of Acidic NOx Emissions from Power Plants with NH_3. *ACS Catal.* **2017**, *7*, 8358–8361. [CrossRef]
5. Reiche, M. Vanadia grafted on TiO_2–SiO_2, TiO_2 and SiO_2 aerogels Structural properties and catalytic behaviour in selective reduction of NO by NH_3. *Appl. Catal. B Environ.* **1999**, *23*, 187–203. [CrossRef]
6. Engweiler, J.; Baiker, A. Vanadia supported on titania aerogels morphological properties and catalytic behaviour in the selective reduction of nitric oxide by ammonia. *Appl. Catal. A Gen.* **1994**, *120*, 187–205. [CrossRef]
7. He, G.; Lian, Z.; Yu, Y.; Yang, Y.; Liu, K.; Shi, X.; Yan, Z.; Shan, W.; He, H. Polymeric vanadyl species determine the low-temperature activity of V-based catalysts for the SCR of NO_x with NH_3. *Sci. Adv.* **2018**, *4*, eaau4637. [CrossRef]
8. Song, I.; Youn, S.; Lee, H.; Lee, S.G.; Cho, S.J.; Kim, D.H. Effects of microporous TiO_2 support on the catalytic and structural properties of V_2O_5/microporous TiO_2 for the selective catalytic reduction of NO by NH_3. *Appl. Catal. B Environ.* **2017**, *210*, 421–431. [CrossRef]
9. Ruff, P.; Schumacher, L.; Rogg, S.; Hess, C. Atomic Layer Deposition-Assisted Synthesis of Embedded Vanadia Catalysts. *ACS Catal.* **2019**, *9*, 6349–6361. [CrossRef]
10. Hess, C. Direct correlation of the dispersion and structure in vanadium oxide supported on silica SBA-15. *J. Catal.* **2007**, *248*, 120–123. [CrossRef]
11. Hess, C. Characterization of the synthesis and reactivity behavior of nanostructured vanadia model catalysts using XPS and vibrational spectroscopy. *Surf. Sci.* **2006**, *600*, 3695–3701. [CrossRef]
12. Hess, C.; Waleska, P.; Ratzka, M.; Janssens, T.V.W.; Rasmussen, S.B.; Beato, P. Hierarchical Vanadia Model Catalysts for Ammonia Selective Catalytic Reduction. *Top. Catal.* **2017**, *60*, 1631–1640. [CrossRef]
13. Segura, Y.; Chmielarz, L.; Kuśtrowski, P.; Cool, P.; Dziembaj, R.; VanSant, E.F. Characterisation and reactivity of vanadia–titania supported SBA-15 in the SCR of NO with ammonia. *Appl. Catal. B Environ.* **2005**, *61*, 69–78. [CrossRef]
14. Lu, J.L.; Elam, J.W.; Stair, P.C. Atomic layer deposition—Sequential self-limiting surface reactions for advanced catalyst "bottom-up" synthesis. *Surf. Sci. Rep.* **2016**, *71*, 410–472. [CrossRef]
15. Johnson, R.W.; Hultqvist, A.; Bent, S.F. A brief review of atomic layer deposition: From fundamentals to applications. *Mater. Today* **2014**, *17*, 236–246. [CrossRef]

16. Miikkulainen, V.; Leskelä, M.; Ritala, M.; Puurunen, R.L. Crystallinity of inorganic films grown by atomic layer deposition: Overview and general trends. *J. Appl. Phys.* **2013**, *113*, 021301. [CrossRef]
17. Li, S.; Xu, J.; Wang, L.; Yang, N.; Ye, X.; Yuan, X.; Xiang, H.; Liu, C.; Li, H. Effect of post-deposition annealing on atomic layer deposited SiO_2 film for silicon surface passivation. *Mater. Sci. Semicond. Process.* **2020**, *106*. [CrossRef]
18. Fares, C.; Islam, Z.; Haque, A.; Kneiß, M.; Von Wenckstern, H.; Grundmann, M.; Tadjer, M.; Ren, F.; Pearton, S.J. Effect of Annealing on the Band Alignment of ALD SiO_2 on $(Al_xGa_{1-x})_2O_3$ for x = 0.2–0.65. *ECS J. Solid State Sci. Technol.* **2019**, *8*, P751–P756. [CrossRef]
19. Ding, Y.; Zhang, Y.; Ren, Y.M.; Orkoulas, G.; Christofides, P.D. Machine learning-based modeling and operation for ALD of SiO_2 thin-films using data from a multiscale CFD simulation. *Chem. Eng. Res. Des.* **2019**, *151*, 131–145. [CrossRef]
20. Fengler, S.; Kriegel, H.; Schieda, M.; Gutzmann, H.; Klassen, T.; Wollgarten, M.; Dittrich, T. Charge Transfer in c-Si(n++)/TiO_2(ALD) at the Amorphous/Anatase Transition: A Transient Surface Photovoltage Spectroscopy Study. *ACS Appl. Mater. Interfaces* **2020**, *12*, 3140–3149. [CrossRef]
21. Yang, Y.; Wei, W.; Wang, S.; Huang, T.; Yuan, M.; Zhang, R.; Yang, W.; Zhang, T.; Sun, Y.; Yuan, Y.J.; et al. Suppression of Photoinduced Surface Oxidation of Vanadium Dioxide Nanostructures by Blocking Oxygen Adsorption. *ACS Omega* **2019**, *4*, 17735–17740. [CrossRef] [PubMed]
22. Hirschberg, C.; Jensen, N.S.; Boetker, J.; Madsen, A.; Kääriäinen, T.O.; Kaariainen, M.-L.; Hoppu, P.; George, S.M.; Murtomaa, M.; Sun, C.C.; et al. Improving Powder Characteristics by Surface Modification Using Atomic Layer Deposition. *Org. Process. Res. Dev.* **2019**, *23*, 2362–2368. [CrossRef]
23. Kim, T.W.; Uchida, S.; Kondo, T.; Segawa, H. Optimization of TiO_2 compact layer formed by atomic layer deposition for efficient perovskite solar cells. *Appl. Phys. Lett.* **2019**, *115*, 203902. [CrossRef]
24. Jo, W.J.; Katsoukis, G.; Frei, H. Ultrathin Amorphous Silica Membrane Enhances Proton Transfer across Solid-to-Solid Interfaces of Stacked Metal Oxide Nanolayers while Blocking Oxygen. *Adv. Funct. Mater.* **2020**, *30*. [CrossRef]
25. Yang, G.Q.; Wang, H.; Gong, T.; Song, Y.H.; Feng, H.; Ge, H.Q.; Ge, H.B.; Liu, Z.T.; Liu, Z.W. Understanding the active-site nature of vanadia-based catalysts for oxidative dehydrogenation of ethylbenzene with CO_2 via atomic layer deposited VOx on γ-Al_2O_3. *J. Catal.* **2019**, *380*, 195–203. [CrossRef]
26. Samek, I.A.; Bobbitt, N.S.; Snurr, R.Q.; Stair, P.C. Interactions of VOx Species with Amorphous TiO_2 Domains on ALD-Derived Alumina-Supported Materials. *J. Phys. Chem. C* **2018**, *123*, 7988–7999. [CrossRef]
27. Song, G.Y.; Oh, C.; Sinha, S.; Son, J.; Heo, J. Facile Phase Control of Multivalent Vanadium Oxide Thin Films (V_2O_5 and VO_2) by Atomic Layer Deposition and Postdeposition Annealing. *ACS Appl. Mater. Interfaces* **2017**, *9*, 23909–23917. [CrossRef]
28. Held, A.; Kowalska-Kuś, J.; Millot, Y.; Averseng, F.; Calers, C.; Valentin, L.; Dzwigaj, S. Influence of the Preparation Procedure of Vanadium-Containing SiBEA Zeolites on Their Catalytic Activity in Propene Epoxidation. *J. Phys. Chem. C* **2018**, *122*, 18570–18582. [CrossRef]
29. Keränen, J.; Guimon, C.; Auroux, A.; Iiskola, E.I.; Niinistö, L. Gas-phase synthesis, structure and surface acid–base properties of highly dispersed vanadia/titania/silica catalysts. *Phys. Chem. Chem. Phys.* **2003**, *5*, 5333–5342. [CrossRef]
30. Keränen, J.; Guimon, C.; Iiskola, E.; Auroux, A.; Niinistö, L. Atomic layer deposition and surface characterization of highly dispersed titania/silica-supported vanadia catalysts. *Catal. Today* **2003**, *78*, 149–157. [CrossRef]
31. Lei, Z.; Long, A.; Wen, C.; Zhang, J.; Chen, B. Experimental and Kinetic Study of Low Temperature Selective Catalytic Reduction of NO with NH_3 over the V_2O_5/AC Catalyst. *Ind. Eng. Chem. Res.* **2011**, *50*, 5360–5368. [CrossRef]
32. Jiang, Y.; Gao, X.; Zhang, Y.; Wu, W.; Luo, Z.; Cen, K. $PbCl_2$-poisoning kinetics of V_2O_5/TiO_2 catalysts for the selective catalytic reduction of NO with NH_3. *Environ. Prog. Sustain. Energy* **2015**, *34*, 1085–1091. [CrossRef]
33. Yang, S.; Wang, C.; Ma, L.; Peng, Y.; Qu, Z.; Yan, N.; Chen, J.; Chang, H.; Li, J. Substitution of WO_3 in V_2O_5/WO3–TiO_2 by Fe_2O_3 for selective catalytic reduction of NO with NH_3. *Catal. Sci. Technol.* **2013**, *3*, 161–168. [CrossRef]
34. Topsøe, N.Y.; Anstrom, M.; Dumesic, J. Raman, FTIR and Theoretical Evidence for Dynamic Structural Rearrangements of Vanadia/Titania $DeNO_x$ Catalysts. *Catal. Lett.* **2001**, *76*, 11–20. [CrossRef]

35. Damma, D.; Ettireddy, P.R.; Reddy, B.M.; Smirniotis, P.G. A review of low temperature NH_3-SCR for removal of NO_x. *Catalysts* **2019**, *9*, 349. [CrossRef]
36. Han, L.; Cai, S.; Gao, M.; Hasegawa, J.Y.; Wang, P.; Zhang, J.; Shi, L.; Zhang, D. Selective Catalytic Reduction of NO_x with NH_3 by Using Novel Catalysts: State of the Art and Future Prospects. *Chem. Rev.* **2019**, *119*, 10916–10976. [CrossRef]
37. Topsoe, N. Characterization of the nature of surface sites on vanadia-titania catalysts by FTIR. *J. Catal.* **1991**, *128*, 499–511. [CrossRef]
38. Topsoe, N.Y.; Dumesic, J.A.; Topsoe, H. Vanadia-titania catalysts for selective catalytic reduction of nitric-oxide by ammonia: II Studies of active sites and formulation of catalytic cycles. *J. Catal.* **1995**, *151*, 241–252. [CrossRef]
39. Topsøe, N.Y.; Slabiak, T.; Clausen, B.S.; Srnak, T.Z.; Dumesic, J.A. Influence of water on the reactivity of vanadia/titania for catalytic reduction of NO_x. *J. Catal.* **1992**, *134*, 742–746. [CrossRef]
40. Topsøe, N.Y.; Topsøe, H. Combined in-situ FTIR and on-line activity studies: Applications to vanadia-titania $DeNO_x$ catalyst. *Catal. Today* **1991**, *9*, 77–82. [CrossRef]
41. Ramis, G.; Yi, L.; Busca, G. Ammonia activation over catalysts for the selective catalytic reduction of NO_x and the selective catalytic oxidation of NH_3. An FT-IR study. *Catal. Today* **1996**, *28*, 373–380. [CrossRef]
42. Marberger, A.; Ferri, D.; Elsener, M.; Kröcher, O. The Significance of Lewis Acid Sites for the Selective Catalytic Reduction of Nitric Oxide on Vanadium-Based Catalysts. *Angew. Chem. Int. Ed.* **2016**, *55*, 11989–11994. [CrossRef] [PubMed]
43. Marberger, A.; Ferri, D.; Elsener, M.; Sagar, A.; Artner, C.; Schermanz, K.; Kröcher, O. Relationship between structures and activities of supported metal vanadates for the selective catalytic reduction of NO by NH_3. *Appl. Catal. B Environ.* **2017**, *218*, 731–742. [CrossRef]
44. Zhu, M.; Lai, J.K.; Tumuluri, U.; Wu, Z.; Wachs, I.E. Nature of Active Sites and Surface Intermediates during SCR of NO with NH_3 by Supported V_2O_5–WO_3/TiO_2 Catalysts. *J. Am. Chem. Soc.* **2017**, *139*, 15624–15627. [CrossRef]
45. Risse, T.; Hollmann, D.; Brückner, A. Chapter 1. In situ electron paramagnetic resonance (EPR)—A unique tool for analysing structure and reaction behaviour of paramagnetic sites in model and real catalysts. *Catalysists* **2015**, *27*, 1–32. [CrossRef]
46. Silversmit, G.; Poelman, H.; Sack, I.; Buyle, G.; Marin, G.B.; De Gryse, R. An in-situ Reduction/Oxidation XAS Study on the EL10V8 VOx/TiO_2(Anatase) Powder Catalyst. *Catal. Lett.* **2006**, *107*, 61–71. [CrossRef]
47. Silversmit, G.; Van Bokhoven, J.A.; Poelman, H.; Van Dereerden, A.; Marin, G.B.; Reyniers, M.; De Gryse, R. The Structure of a VOxTiO_2anatase Powder Catalyst under Reduction and Oxidation at 623K. *Phys. Scr.* **2005**, *115*, 798. [CrossRef]
48. Silversmit, G.; Van Bokhoven, J.A.; Poelman, H.; Van Der Eerden, A.M.; Marin, G.B.; Reyniers, M.F.; De Gryse, R. The structure of supported and unsupported vanadium oxide under calcination, reduction and oxidation determined with XAS. *Appl. Catal. A Gen.* **2005**, *285*, 151–162. [CrossRef]
49. Feng, H.; Elam, J.W.; Libera, J.A.; Pellin, M.J.; Stair, P.C. Oxidative dehydrogenation of cyclohexane over alumina-supported vanadium oxide nanoliths. *J. Catal.* **2010**, *269*, 421–431. [CrossRef]
50. Feng, Z.; Lu, J.; Feng, H.; Stair, P.C.; Elam, J.W.; Bedzyk, M.J. Catalysts Transform While Molecules React: An Atomic-Scale View. *J. Phys. Chem. Lett.* **2013**, *4*, 285–291. [CrossRef]
51. Feng, Z.; Cheng, L.; Kim, C.Y.; Elam, J.W.; Zhang, Z.; Curtiss, L.A.; Zapol, P.; Bedzyk, M.J. Atomic-Scale Study of Ambient-Pressure Redox-Induced Changes for an Oxide-Supported Submonolayer Catalyst: VO_x/α-TiO_2(110). *J. Phys. Chem. Lett.* **2012**, *3*, 2845–2850. [CrossRef]
52. Arnarson, L.; Rasmussen, S.B.; Falsig, H.; Lauritsen, J.V.; Moses, P.G. Coexistence of Square Pyramidal Structures of Oxo Vanadium (+5) and (+4) Species Over Low-Coverage VO_X/TiO_2 (101) and (001) Anatase Catalysts. *J. Phys. Chem. C* **2015**, *119*, 23445–23452. [CrossRef]
53. Avdeev, V.I.; Bedilo, A.F. Molecular mechanism of propane oxidative dehydrogenation on surface oxygen radical sites of VO_x/TiO_2 catalysts. *Res. Chem. Intermed.* **2015**, *42*, 5237–5252. [CrossRef]
54. Avdeev, V.I.; Bedilo, A.F. Molecular Mechanism of Oxygen Isotopic Exchange over Supported Vanadium Oxide Catalyst VO_x/TiO_2. *J. Phys. Chem. C* **2013**, *117*, 2879–2887. [CrossRef]
55. Avdeev, V.I.; Tapilin, V.M. Water Effect on the Electronic Structure of Active Sites of Supported Vanadium Oxide Catalyst VO_x/TiO_2(001). *J. Phys. Chem. C* **2010**, *114*, 3609–3613. [CrossRef]

56. Jehng, J.-M.; Deo, G.; Weckhuysen, B.M.; Wachs, I.E. Effect of water vapor on the molecular structures of supported vanadium oxide catalysts at elevated temperatures. *J. Mol. Catal. A Chem.* **1996**, *110*, 41–54. [CrossRef]
57. Ruff, P.; Lauterbach, S.; Kleebe, H.J.; Hess, C. Surface structuring of mesoporous materials by controlled synthesis of nanocavities. *Microporous Mesoporous Mater.* **2016**, *235*, 160–169. [CrossRef]
58. Thielemann, J.P.; Girgsdies, F.; Schlögl, R.; Hess, C. Pore structure and surface area of silica SBA-15: Influence of washing and scale-up. *Beilstein J. Nanotechnol.* **2011**, *2*, 110–118. [CrossRef]
59. Huang, Y.; Gao, D.; Tong, Z.; Zhang, J.; Luo, H. Oxidation of NO over cobalt oxide supported on mesoporous silica. *J. Nat. Gas Chem.* **2009**, *18*, 421–428. [CrossRef]
60. Lubas, M.; Jasinski, J.; Sitarz, M.; Kurpaska, L.; Podsiad, P. Raman spectroscopy of TiO_2 thin films formed by hybrid treatment for biomedical applications. *Spectrochim. Acta Part A Mol. Biomol. Spectrosc.* **2014**, *133*, 867–871. [CrossRef]
61. Zhang, Q.; Ma, L.; Shao, M.; Huang, J.; Ding, M.; Deng, X.; Wei, X.; Xu, X. Anodic Oxidation Synthesis of One-Dimensional TiO_2Nanostructures for Photocatalytic and Field Emission Properties. *J. Nanomater.* **2014**, *2014*, 1–14. [CrossRef]
62. Waleska, P.S.; Rupp, S.; Hess, C. Operando Multiwavelength and Time-Resolved Raman Spectroscopy: Structural Dynamics of a Supported Vanadia Catalyst at Work. *J. Phys. Chem. C* **2018**, *122*, 3386–3400. [CrossRef]
63. Tallant, D.R.; Bunker, B.C.; Balfe, C.A.; Brinker, C.J. Raman Spectra of Rings in Silicate Materials. *MRS Proc.* **1986**, *73*, 261. [CrossRef]
64. Chligui, M.; Guimbretiere, G.; Canizares, A.; Matzen, G.; Vaills, Y.; Simon, P. New Features in the Raman Spectrum of Silica: Key-Points in the Improvement on Structure Knowledge. Available online: https://hal.archives-ouvertes.fr/hal-00520823/document (accessed on 27 November 2020).
65. Huang, T.; Hu, Z.; Xu, G.S.; Zhang, X.L.; Zhang, J.Z.; Chu, J.H. Inherent optical behavior and structural variation in $Na_{0.5}Bi_{0.5}TiO_3$-6%$BaTiO_3$ revealed by temperature dependent Raman scattering and ultraviolet-visible transmittance. *Appl. Phys. Lett.* **2014**, *104*, 111908. [CrossRef]
66. Kreisel, J.; Glazer, A.M.; Jones, G.; Thomas, P.A.; Abello, L.; Lucazeau, G. An x-ray diffraction and Raman spectroscopy investigation of A-site substituted perovskite compounds: The $(Na_{1-x}K_x)_{0.5}Bi_{0.5}TiO_3$(0lexle1) solid solution. *J. Phys. Condens. Matter* **2000**, *12*, 3267–3280. [CrossRef]
67. Walrafen, G.E.; Chu, Y.C.; Hokmabadi, M.S. Raman spectroscopic investigation of irreversibly compacted vitreous silica. *J. Chem. Phys.* **1990**, *92*, 6987–7002. [CrossRef]
68. Li, C.; Xiong, G.; Liu, J.; Ying, P.; Xin, A.Q.; Feng, Z. Identifying Framework Titanium in TS-1 Zeolite by UV Resonance Raman Spectroscopy. *J. Phys. Chem. B* **2001**, *105*, 2993–2997. [CrossRef]
69. Hess, C.; Tzolova-Müller, G.; Herbert, R. The Influence of Water on the Dispersion of Vanadia Supported on Silica SBA-15: A Combined XPS and Raman Study. *J. Phys. Chem. C* **2007**, *111*, 9471–9479. [CrossRef]
70. Eberhardt, M.A.; Proctor, A.; Houalla, M.; Hercules, D.M. Investigation of V Oxidation States in Reduced V/Al2O3Catalysts by XPS. *J. Catal.* **1996**, *160*, 27–34. [CrossRef]
71. Sawatzky, G.A.; Post, D. X-ray photoelectron and Auger spectroscopy study of some vanadium oxides. *Phys. Rev. B* **1979**, *20*, 1546–1555. [CrossRef]
72. Pan, Y.; Zhao, W.; Zhong, Q.; Cai, W.; Li, H. Promotional effect of Si-doped V_2O_5/TiO_2 for selective catalytic reduction of NO x by NH_3. *J. Environ. Sci.* **2013**, *25*, 1703–1711. [CrossRef]
73. Gao, X.; Bare, S.R.; Fierro, J.L.G.; Wachs, I.E. Structural Characteristics and Reactivity/Reducibility Properties of Dispersed and Bilayered $V_2O_5/TiO_2/SiO_2$ Catalysts. *J. Phys. Chem. B* **1999**, *103*, 618–629. [CrossRef]
74. Nitsche, D.; Hess, C. Structure of Isolated Vanadia and Titania: A Deep UV Raman, UV–Vis, and IR Spectroscopic Study. *J. Phys. Chem. C* **2016**, *120*, 1025–1037. [CrossRef]
75. Waleska, P.; Hess, C. Structural Dynamics of Dispersed Titania During Dehydration and Oxidative Dehydrogenation Studied by In Situ UV Raman Spectroscopy. *Catal. Lett.* **2018**, *148*, 2537–2547. [CrossRef]
76. Gao, X.; Bare, S.R.; Fierro, J.L.G.; Banares, M.A.; Wachs, I.E. Preparation and in-Situ Spectroscopic Characterization of Molecularly Dispersed Titanium Oxide on Silica. *J. Phys. Chem. B* **1998**, *102*, 5653–5666. [CrossRef]
77. Beck, B.; Harth, M.; Hamilton, N.G.; Carrero, C.A.; Uhlrich, J.J.; Trunschkec, A.; Shaikhutdinov, S.; Schubert, H.; Freund, H.; Schlögl, R.; et al. Partial oxidation of ethanol on vanadia catalysts on supporting oxides with different redox properties compared to propane. *J. Catal.* **2012**, *296*, 120–131. [CrossRef]

78. Schraml-Marth, M.; Pohl, M.; Krauss, H.-L.; Wokaun, A. Spectroscopic investigation of the structure of silica-supported vanadium oxide catalysts at submonolayer coverages. *J. Chem. Soc. Faraday Trans.* **1991**, *87*, 2635–2646. [CrossRef]
79. Arena, F.; Frusteri, F.; Martra, G.; Coluccia, S.; Parmaliana, A. Surface structures, reduction pattern and oxygen chemisorption of V_2O_5/SiO_2 catalysts. *J. Chem. Soc. Faraday Trans.* **1997**, *93*, 3849–3854. [CrossRef]
80. Kwon, D.W.; Park, K.H.; Hong, S.C. Influence of VO x surface density and vanadyl species on the selective catalytic reduction of NO by NH_3 over VO_x/TiO_2 for superior catalytic activity. *Appl. Catal. A Gen.* **2015**, *499*, 1–12. [CrossRef]
81. Burcham, L.J.; Deo, G.; Gao, X.; Wachs, I.E. In situ IR, Raman, and UV-Vis DRS spectroscopy of supported vanadium oxide catalysts during methanol oxidation. *Top. Catal.* **2000**, *11*, 85–100. [CrossRef]
82. Gao, X.; Wachs, I.E. Investigation of Surface Structures of Supported Vanadium Oxide Catalysts by UV−vis−NIR Diffuse Reflectance Spectroscopy. *J. Phys. Chem. B* **2000**, *104*, 1261–1268. [CrossRef]
83. Srinivas, D.; Hölderich, W.; Kujath, S.; Valkenberg, M.; Raja, T.; Saikia, L.; Hinze, R.; Ramaswamy, V. Active sites in vanadia/titania catalysts for selective aerial oxidation of β-picoline to nicotinic acid. *J. Catal.* **2008**, *259*, 165–173. [CrossRef]
84. Due-Hansen, J.; Rasmussen, S.B.; Mikolajska, E.; Bañares, M.A.; Avila, P.C.; Fehrmann, R. Redox behaviour of vanadium during hydrogen–oxygen exposure of the V_2O_5-WO_3/TiO_2 SCR catalyst at 250 °C. *Appl. Catal. B Environ.* **2011**, *107*, 340–346. [CrossRef]
85. Davis, E.A.; Mott, N.F. Conduction in non-crystalline systems V. Conductivity, optical absorption and photoconductivity in amorphous semiconductors. *Philos. Mag.* **1970**, *22*, 0903–0922. [CrossRef]
86. Ghosh, A.; Bhattacharya, S. Optical and other physical properties of semiconducting cadmium vanadate glasses. *J. Appl. Phys.* **2007**, *101*, 83511. [CrossRef]
87. Tauc, J. Absorption edge and internal electric fields in amorphous semiconductors. *Mater. Res. Bull.* **1970**, *5*, 721–729. [CrossRef]
88. Waleska, P.S.; Hess, C. Oligomerization of Supported Vanadia: Structural Insight Using Surface-Science Models with Chemical Complexity. *J. Phys. Chem. C* **2016**, *120*, 18510–18519. [CrossRef]
89. Borovkov, V.Y.; Mikheeva, E.P.; Zhidomirov, G.M.; Lapina, O.B. Theoretical and Experimental Studies of the Nature of the Catalytic Activity of VO_x/TiO_2 Systems. *Kinet. Catal.* **2003**, *44*, 710–717. [CrossRef]
90. Bulushev, D.A.; Reshetnikov, S.I.; Kiwi-Minsker, L.; Renken, A. Deactivation kinetics of V/Ti-oxide in toluene partial oxidation. *Appl. Catal. A Gen.* **2001**, *220*, 31–39. [CrossRef]
91. Kamata, H. The role of K_2O in the selective reduction of NO with NH_3 over a $V_2O_5(WO_3)/TiO_2$ commercial selective catalytic reduction catalyst. *J. Mol. Catal. A Chem.* **1999**, *139*, 189–198. [CrossRef]
92. Lu, J.; Kosuda, K.M.; Van Duyne, R.P.; Stair, P.C. Surface Acidity and Properties of TiO_2/SiO_2 Catalysts Prepared by Atomic Layer Deposition: UV−visible Diffuse Reflectance, DRIFTS, and Visible Raman Spectroscopy Studies. *J. Phys. Chem. C* **2009**, *113*, 12412–12418. [CrossRef]
93. Mu, J.C.; Li, X.Y.; Sun, W.B.; Fan, S.Y.; Wang, X.Y.; Wang, L.; Qin, M.C.; Gan, G.Q.; Yin, Z.F.; Zhang, D.K. Inductive Effect Boosting Catalytic Performance of Advanced $Fe_{1-x}V_xO$ delta Catalysts in Low-Temperature NH_3 Selective Catalytic Reduction: Insight into the Structure, Interaction, and Mechanisms. *ACS Catal.* **2018**, *8*, 6760–6774. [CrossRef]
94. Cheng, K.; Liu, J.; Zhao, Z.; Wei, Y.; Jiang, G.; Duan, A. Direct synthesis of V–W–Ti nanoparticle catalysts for selective catalytic reduction of NO with NH_3. *RSC Adv.* **2015**, *5*, 45172–45183. [CrossRef]
95. Zhu, L.; Zhong, Z.; Yang, H.; Wang, C. Effect of MoO_3 on vanadium based catalysts for the selective catalytic reduction of NO_x with NH_3 at low temperature. *J. Environ. Sci.* **2017**, *56*, 169–179. [CrossRef]
96. Topsoe, N.; Topsoe, H.; Dumesic, J.A. Vanadia/Titania Catalysts for Selective Catalytic Reduction (SCR) of Nitric-Oxide by Ammonia. *J. Catal.* **1995**, *151*, 226–240. [CrossRef]
97. Anstrom, M. Density functional theory studies of mechanistic aspects of the SCR reaction on vanadium oxide catalysts. *J. Catal.* **2003**, *213*, 115–125. [CrossRef]
98. Farber, M.; Harris, S.P. Kinetics of ammonia-nitric oxide reactions on vanadium oxide catalysts. *J. Phys. Chem.* **1984**, *88*, 680–682. [CrossRef]
99. Bredow, T.; Homann, T.; Jug, K. Adsorption of NO, NH_3 and H_2O on V_2O_5/TiO_2 catalysts. *Res. Chem. Intermed.* **2004**, *30*, 65–73. [CrossRef]

100. Yao, H.; Chen, Y.; Zhao, Z.; Wei, Y.; Liu, Z.; Zhai, D.; Liu, B.; Xu, C. Periodic DFT study on mechanism of selective catalytic reduction of NO via NH_3 and O_2 over the V_2O_5 (001) surface: Competitive sites and pathways. *J. Catal.* **2013**, *305*, 67–75. [CrossRef]
101. Nickl, J.; Dutoit, D.; Baiker, A.; Scharf, U.; Wokaun, A. Vanadia catalysts for the selective catalytic reduction of NO by NH_3 prepared by vapour deposition of vanadyl alkoxide onto various supports. *Ber. Bunsenges. Phys. Chem.* **1993**, *97*, 217–228.
102. Pinaeva, L.; Suknev, A.; Budneva, A.; Paukshtis, E.; Bal'Zhinimaev, B. On the role of oxygen in the reaction of NO reduction by NH_3 over monolayer V_2O_5 TiO_2 catalyst. *J. Mol. Catal. A Chem.* **1996**, *112*, 115–124. [CrossRef]
103. Mihai, O.; Creaser, D.; Olsson, L. Adsorption and Oxidation Investigations over Pt/Al_2O_3 Catalyst: A Microcalorimetric Study. *Catalists* **2016**, *6*, 73. [CrossRef]
104. Zhang, S.; Zhang, B.; Liu, B.; Sun, S. A review of Mn-containing oxide catalysts for low temperature selective catalytic reduction of NO_x with NH_3: Reaction mechanism and catalyst deactivation. *RSC Adv.* **2017**, *7*, 26226–26242. [CrossRef]
105. Klyushina, A.; Pacultová, K.; Karásková, K.; Jirátová, K.; Ritz, M.; Fridrichová, D.; Volodarskaja, A.; Obalová, L. Effect of preparation method on catalytic properties of Co-Mn-Al mixed oxides for N_2O decomposition. *J. Mol. Catal. A Chem.* **2016**, *425*, 237–247. [CrossRef]
106. Hamilton, N.; Wolfram, T.; Müller, G.T.; Hävecker, M.; Kröhnert, J.; Carrero, C.; Schomäcker, R.; Trunschkec, A.; Schlögl, R. Topology of silica supported vanadium–titanium oxide catalysts for oxidative dehydrogenation of propane. *Catal. Sci. Technol.* **2012**, *2*, 1346–1359. [CrossRef]
107. Deo, G.; Wachs, I. Effect of Additives on the Structure and Reactivity of the Surface Vanadium Oxide Phase in V_2O_5/TiO_2 Catalysts. *J. Catal.* **1994**, *146*, 335–345. [CrossRef]
108. Jehng, J.M.; Wachs, I.E. The molecular structures and reactivity of $V_2O_5/TiO_2/SiO_2$ catalysts. *Catal. Lett.* **1992**, *13*, 9–19. [CrossRef]
109. Rouquerol, F.O.; Rouquerol, J.; Sing, K.S.W.; Llewellyn, P.L.; Maurin, G. *Adsorption by Powders and Porous Solids: Principles, Methodology and Applications*, 2nd ed.; Elsevier/AP: Amsterdam, The Netherlands, 2014.
110. Haber, J.; Machej, T.; Czeppe, T. The phenomenon of wetting at solid/solid interface. *Surf. Sci.* **1985**, *151*, 301–310. [CrossRef]
111. Wang, C.B.; Cai, Y.; Wachs, I.E. Reaction-Induced Spreading of Metal Oxides onto Surfaces of Oxide Supports during Alcohol Oxidation: Phenomenon, Nature, and Mechanisms. *Langmuir* **1999**, *15*, 1223–1235. [CrossRef]
112. Zhu, H.; Ould-Chikh, S.; Dong, H.; Llorens, I.; Saih, Y.; Anjum, D.H.; Hazemann, J.L.; Basset, J.M. VO_x/SiO_2Catalyst Prepared by Grafting $VOCl_3$ on Silica for Oxidative Dehydrogenation of Propane. *Chem. Cat. Chem.* **2015**, *7*, 3332–3339. [CrossRef]
113. Moisii, C.; Curran, M.D.; Van De Burgt, L.J.; Stiegman, A.E. Raman spectroscopy of discrete silica supported vanadium oxide: Assignment of fundamental stretching modes. *J. Mater. Chem.* **2005**, *15*, 3519–3524. [CrossRef]
114. Nuguid, R.J.G.; Ferri, D.; Marberger, A.; Nachtegaal, M.; Kröcher, O. Modulated Excitation Raman Spectroscopy of V_2O_5/TiO_2: Mechanistic Insights into the Selective Catalytic Reduction of NO with NH_3. *ACS Catal.* **2019**, *9*, 6814–6820. [CrossRef]
115. Lietti, L.; Alemany, J.L.; Forzatti, P.; Busca, G.; Ramis, G.; Giamello, E.; Bregani, F. Reactivity of V_2O_5-WO_3/TiO_2 catalysts in the selective catalytic reduction of nitric oxide by ammonia. *Catal. Today* **1996**, *29*, 143–148. [CrossRef]
116. Arnarson, L.; Falsig, H.; Rasmussen, S.B.; Lauritsen, J.V.; Moses, P.G. A complete reaction mechanism for standard and fast selective catalytic reduction of nitrogen oxides on low coverage VO /TiO_2(0 0 1) catalysts. *J. Catal.* **2017**, *346*, 188–197. [CrossRef]
117. Giakoumelou, I.; Fountzoula, C.; Kordulis, C.; Boghosian, S. Molecular structure and catalytic activity of V_2O_5/TiO_2 catalysts for the SCR of NO by NH_3: In situ Raman spectra in the presence of O_2, NH_3, NO, H_2, H_2O, and SO_2. *J. Catal.* **2006**, *239*, 1–12. [CrossRef]
118. Dong, L.; Sun, C.; Tang, C.; Zhang, B.; Zhu, J.; Liu, B.; Gao, F.; Hu, Y.; Dong, L.; Chen, Y. Investigations of surface VO_x species and their contributions to activities of $VO_x/Ti_{0.5}Sn_{0.5}O_2$ catalysts toward selective catalytic reduction of NO by NH_3. *Appl. Catal. A Gen.* **2012**, *431*, 126–136. [CrossRef]

119. Zhang, Q.M.; Song, C.; Lyu, G.; Bin, F.; Pang, H.T.; Song, J. Effect of metal oxide partial substitution of V_2O_5 in V_2O_5–WO_3/TiO_2 on selective catalytic reduction of NO with NH_3. *J. Ind. Eng. Chem.* **2015**, *24*, 79–86. [CrossRef]
120. Zhang, S.; Zhong, Q. Promotional effect of WO_3 on O_2^- over V_2O_5/TiO_2 catalyst for selective catalytic reduction of NO with NH_3. *J. Mol. Catal. A Chem.* **2013**, *373*, 108–113. [CrossRef]
121. Wang, P.; Guo, R.T. The promotion effect of copper doping on the potassium resistance of V/TiO_2 catalyst for selective catalytic reduction of NO with NH_3. *Chem. Pap.* **2017**, *71*, 2253–2259. [CrossRef]
122. Handy, B.E.; Baiker, A.; Schraml-Marth, M.; Wokaun, A. Vanadia supported on TiO_2-SiO_2 mixed oxide gels: Structure of the dispersed phase and activity for the selective catalytic reduction of NO with NH_3. *J. Catal.* **1992**, *133*, 1–20. [CrossRef]
123. Handy, B.E.; Maciejewski, M.; Baiker, A. Vanadia, vanadia-titania, and vanadia-titania-silica gels: Structural genesis and catalytic behavior in the reduction of nitric oxide with ammonia. *J. Catal.* **1992**, *134*, 75–86. [CrossRef]
124. Kobayashi, M.; Kuma, R.; Masaki, S.; Sugishima, N. TiO_2-SiO_2 and V_2O_5/TiO_2-SiO_2 catalyst: Physico-chemical characteristics and catalytic behavior in selective catalytic reduction of NO by NH_3. *Appl. Catal. B Environ.* **2005**, *60*, 173–179. [CrossRef]
125. Won, J.M.; Kim, M.S.; Hong, S.C. Effect of vanadium surface density and structure in VOx/TiO_2 on selective catalytic reduction by NH_3. *Korean J. Chem. Eng.* **2018**, *35*, 2365–2378. [CrossRef]
126. Dutoit, D.C.M.; Reiche, M.A.; Baiker, A. Vanadia-silica aerogels—Structure and catalytic properties in selective reduction of NO by NH_3. *Appl. Catal. B-Environ.* **1997**, *13*, 275–288. [CrossRef]
127. Soyer, S.; Uzun, A.; Senkan, S.; Onal, I. A quantum chemical study of nitric oxide reduction by ammonia (SCR reaction) on V_2O_5 catalyst surface. *Catal. Today* **2006**, *118*, 268–278. [CrossRef]
128. Dai, H.; Bell, A.T.; Iglesia, E. Effects of molybdena on the catalytic properties of vanadia domains supported on alumina for oxidative dehydrogenation of propane. *J. Catal.* **2004**, *221*, 491–499. [CrossRef]
129. Zhao, D.; Sun, J.; Li, Q.; Stucky, G.D. Morphological Control of Highly Ordered Mesoporous Silica SBA-15. *Chem. Mater.* **2000**, *12*, 275–279. [CrossRef]